Journal of Hydraulic Research

ISSN: 0022-1686 (Print) 1814-2079 (Online) Journal homepage: http://www.tandfonline.com/loi/tjhr20

High-frequency acoustic wave properties in a water-filled pipe. Part 1: dispersion and multi-path behaviour

Moez Louati & Mohamed S. Ghidaoui

To cite this article: Moez Louati & Mohamed S. Ghidaoui (2017): High-frequency acoustic wave properties in a water-filled pipe. Part 1: dispersion and multi-path behaviour, Journal of Hydraulic Research, DOI: 10.1080/00221686.2017.1354931

To link to this article: http://dx.doi.org/10.1080/00221686.2017.1354931

Published online: 31 Jul 2017.

Submit your article to this journal

View related articles

View Crossmark data

Citing articles: 1 View citing articles

Full Terms & Conditions of access and use can be found at
http://www.tandfonline.com/action/journalInformation?journalCode=tjhr20

Download by: [HKUST Library] **Date:** 31 July 2017, At: 21:10

Journal of Hydraulic Research, 2017
https://doi.org/10.1080/00221686.2017.1354931
© 2017 International Association for Hydro-Environment Engineering and Research

Research paper

High-frequency acoustic wave properties in a water-filled pipe. Part 1: dispersion and multi-path behaviour

MOEZ LOUATI (IAHR Member), Postdoctoral Fellow, *Civil and Environmental Engineering/School of Engineering, The Hong Kong University of Science and Technology, Kowloon, Hong Kong, PR China*
Email: mlouati@connect.ust.hk (author for correspondence)

MOHAMED S. GHIDAOUI (IAHR Member), Chair Professor, *Civil and Environmental Engineering, The Hong Kong University of Science and Technology, Kowloon, Hong Kong, PR China*
Email: ghidaoui@ust.hk

ABSTRACT
Defect resolution using transient-based detection methods (TBDDM) improves as frequency bandwidth of injected signals increases. High-frequency waves (HFW) excite radial and azimuthal modes, however, making the 1D water-hammer ineffective for these phenomena. This paper focuses on idealized HFW in inviscid, slightly compressible fluid in rigid, unbounded, circular conduits. HFW waves are generated by an axisymmetric wave source. High-order 2D finite volume scheme is developed for HFW. Results show that injected probing waves containing a cut-off frequency exhibit significant wave dispersion, and group velocity varies over a wide range of speeds, resulting in wave-energy spatial spreading with large amplitude reduction. Injected signals without any cut-off frequency remain spatially separated. Size of wave source significantly affects energy distribution within wave modes. Practical implications are that probing wave and defect resolution effectiveness may be increased using (i) probing HFW without cut-off frequencies contained in the bandwidth of the injected probing signal, and (ii) larger power sources for the injection of probing wave signals.

Keywords: High-frequency waves; high modes; numerical investigation; pipe system; wave dispersion

1 Introduction

The use of high-frequency acoustic waves (HFW) as a probing tool to provide high-resolution non-destructive and non-invasive defect detection in water supply systems (WSS) is a new research area being investigated for potential use by the authors of this paper together with a large team of international researchers (see http://smartuws.ust.hk/). Owing both to its novelty for use in transient-based defect detection schemes and to the unfamiliarity of most researchers in the TBDDM field to the use of higher frequency transient (acoustic) waves, this introduction is extended to provide a better basis for readers to understand the theoretical underpinnings both for its study and its well-developed theoretical basis in the field of acoustics. This paper deals mainly with preliminary explorations and conclusions regarding the behaviour of idealized HFW and suggests some implications regarding their potential use in water supply systems (WSS). Where necessary for clarity and context, additional details about transient-based defect detection and its limitations in general are discussed.

The studies of water-hammer (WH) phenomena in pipe flows have been undertaken since the middle of the nineteenth century (Chaudhry, 2014). WH arises in a wide range of pipeline applications, including water distribution systems, energy pipelines, power plants, and many others. In the 1990s, researchers became aware that transient (WH) waves in pipelines contained information arising from wave alteration whenever the wave is affected by changes in conduit or boundary properties. The abnormal or anomalous information thus recorded in the altered wave signals became the basis for interpreting changes to the wave signal that could be caused by defects, hence the name given to this approach, i.e. transient-based defect detection methods.

The majority of existing WH models are one-dimensional (1-D), which assumes that the pipe pressure does not vary with radius and that the radial velocity is negligible compared

Received 30 April 2016; accepted 5 July 2017/Currently open for discussion.

ISSN 0022-1686 print/ISSN 1814-2079 online
http://www.tandfonline.com

to the axial velocity (Ghidaoui, 2004). Such models are the workhorses of WH analysis and pipeline design. In the last two decades, quasi-2-D transient models were developed to examine the validity of existing unsteady friction relations and guide the development of new ones (e.g. Eichinger & Lein, 1992; Pezzinga, 1999; Pezzinga, 2000; Silva-Araya & Chaudhry, 1997; Vardy & Hwang, 1991; Zhao & Ghidaoui, 2003). These 2-D models also assume that pipe pressure is not a function of radius. To the authors' knowledge, the only numerical work using a complete 2-D model in which the radial variation of pressure is included is by Mitra and Rouleau (1985), who employed an implicit numerical scheme based on matrix factorization. Specifically, they used a finite difference method (FDM) for space discretization and a three-backward-point scheme for time marching. A predictor-corrector technique was used to sweep along the axial and radial directions simultaneously. They reported that classical 1-D WH theory for laminar flows is invalid in the vicinity of devices (e.g. valves) and singularities. However, their test cases were limited to relatively low wave frequencies. The radial waves in Mitra and Rouleau (1985) are due to the Hagen–Poiseulle velocity, which, if arrested by a valve, produces a WH pressure that varies with radius. In fact, the pressure rise at the centreline is about twice that predicted by the classic Joukowsky expression.

Theoretically, the assumption that the pressure is not a function of radius is valid provided that the frequency of the WH is of the order of a/D or smaller, where a is the wave speed and D is the pipe diameter (e.g. see Rienstra & Hirschberg, 2004 and the brief review provided in Section 2). For example, taking an approximate but typical real-world value of a for steel or concrete pipe ($\approx 1000\,\mathrm{m\,s^{-1}}$) and D (≈ 0.1 to $0.5\,\mathrm{m}$) shows that the classical WH models are valid if the wave frequency, f, is of the order of 2 to 10 kHz or smaller. In the past, this neglect of radial wave velocity, and by implication the classical 1-D WH theory, has been useful and valid because WH waves are generated by mechanical devices such valves and pumps whose frequency is well below 1 kHz. This is not necessarily true for transient-based defect detection methods.

Since the pioneering work of Liggett and Chen (1994), transient-based defect detection methods (TBDDM) were developed in which a known (generally 1-D plane) wave signal is injected into the conduit, and the response (waveform of the propagated and reflected signals) is measured at selected location(s) is processed. TBDDMs are now a useful general approach for defect detection of blockages, leaks, and for overall pipe wall condition assessment (e.g. Brunone & Ferrante, 2001; Covas, Ramos, Brunone, & Young, 2004; Duan et al., 2013; Lee, Duan, Ghidaoui, & Karney, 2013; Lee, Vítkovský, Lambert, Simpson, & Liggett, 2008; Liggett & Chen, 1994; Meniconi et al., 2013; Sattar, Chaudhry, & Kassem, 2008; Vítkovský, Simpson, & Lambert, 2000; Wang, Lambert, & Simpson, 2005; Zhao, Duan, & Ghidaoui, 2016) (the list of important papers is long and is included in the reference section although not all papers are cited here). The basic principle involved is that a measured wave signal in a fluid-filled conduit is modified by, and thus contains information about, the conduit's properties and state. In fact, wave theory is widely used to probe and characterize various media and to convey information in various applications (e.g. non-destructive material testing, medical diagnostics, and underwater communications), where it is well known that higher frequency probing waves produce better resolution of the system state, including its identifiable defects. Unsurprisingly, similar conclusions are found for TBDDM (e.g. Lee, Duan, Tuck, & Ghidaoui, 2015; Louati & Ghidaoui, 2015). In fact, probing waves cannot resolve pipe properties, condition or defects at scales smaller than a/f. For example, simulated sudden pipe bursts could only be located to within $\pm 45\,\mathrm{m}$ (i.e. 90 m range) even though a sensor was located only 20 m away from the defect (Allen et al., 2011). The wave resolution in Allen's case is $a/f \approx 900/10 \approx 90\,\mathrm{m}$. In addition, a simulated burst in Hong Kong could only be located to within $\pm 42\,\mathrm{m}$ (Hong Kong Water Supplies Department (WSD), private communication). The minimum wave resolution in this case is $a/f \approx 1200/10$ which is close to 90 m. In Milan, Italy, leaks could only be located to within 800 m (Meniconi et al., 2015). The wave resolution in this case is $a/f \approx 900/1 \approx 900\,\mathrm{m}$.

High-frequency piezoelectric actuators are widely used in underwater acoustics applications, but are rarely used in the study of fluid transients. Currently, the authors are conducting preliminary WH tests generated by piezoelectric actuators with a frequency bandwidth up to 100 kHz, which is well beyond the scope of this paper but will be discussed in future work. Such frequencies excite radial waves and are beyond the range of validity of the classical WH theory. Although the theory of high-frequency WH waves is not presently developed, the physics of acoustic waves in gas/air flows is already advanced and is founded on many early notable works (e.g. Anderson & Barnes, 1953; Hartig & Swanson, 1938; Miles, 1944; Rochester, 1941). A good summary of key analytical treatment of acoustic wave propagation in cylindrical gas-filled tubes is given in Tijdeman (1975). A recent experiment conducted by Kokossalakis (2006) for the purpose of communication system design for in-pipe wireless sensor network injected high-frequency waves and collected the propagated signals at separate locations in a variety of test pipe set-ups. Although the experiment was conducted in air-filled pipes, the parameters in the experiment were scaled to mimic wave propagation in a water-filled pipe.

In Part 1 of this work (this paper), fundamental theoretical and numerical results for high-frequency waves in a water-filled pipe are briefly reviewed. Additionally, a two-dimensional model for high-frequency WH waves is developed and applied to water-filled pipe flow to study the fundamental, idealized behaviour of high-frequency waves in water pipes. This paper focuses on the analysis and description of dispersion behaviour in HFW and considers only inviscid flow in a single infinite pipe system with initial condition of zero (stagnant) flow. Part 2 (this issue) studies the effect of fluid viscosity and focuses on the propagation range of HFW. It gives preliminary insights

into the physical and behavioural factors that practitioners may need to take into account if HFW are to be successfully used for TBDDM.

2 Review of the basic properties of the wave solution

2.1 *2-D pressure wave solution*

Let x and r denote the axial and radial coordinates in a cylindrical coordinate system; t is the time; P denotes the fluid pressure; and a is the speed of sound in the fluid. If the convective terms (i.e. the analysis for small Mach number), the body forces and the viscous forces can be neglected, the following wave equation is given (Rienstra & Hirschberg, 2004):

$$\frac{\partial^2 P}{\partial t^2} - a^2 \nabla^2 P = 0 \tag{1}$$

where ∇^2 is the Laplace operator. For steady oscillatory (stagnant) flow in a straight rigid pipe, Eq. (1) has the following analytical solution (details of the solution can be found in Rienstra & Hirschberg, 2004):

$$P = \sum_n P_n = \sum_n [\varphi_n \exp(ik_{xn}x - iwt) + \gamma_n \exp(-ik_{xn}x - iwt)]J_0(rk_{rn}) \tag{2}$$

where

$$k_{xn} = \sqrt{(w/a)^2 - k_{rn}^2} \quad \text{and} \quad k_{rn} = \frac{\alpha_{rn}}{R} \tag{3}$$

α_{rn} is the nth zero of $\partial J_0(rk_{rn})/\partial r = 0$ (at $r = R$) which results from imposing the no-flux condition at the pipe wall and gives $\alpha_{rn} = 0,\ 3.8317,\ 7.01556, \ldots$, etc. In the above, J_0 is the Bessel function of the first kind of order 0; R is the pipe radius; $w = 2\pi f$ is the angular frequency (in rad s^{-1}) with f the frequency (in Hz); and φ_n and γ_n are respectively the amplitudes of the nth mode of the left and right going waves along the pipe.

2.2 *Basic properties of the wave solution*

The pressure of the left going nth mode wave is:

$$P_n = \varphi_n \exp(ik_{xn}x - iwt)J_0(rk_{rn}) \tag{4}$$

It is clear from Eqs (3) and (4) that:

$$\begin{cases} \text{if} \quad k^2 > k_{rn}^2 \Rightarrow \sqrt{k^2 - k_{rn}^2} \text{ is real} \\ \qquad\qquad \Rightarrow \text{Propagating mode} \\ \text{if} \quad k^2 < k_{rn}^2 \Rightarrow \sqrt{k^2 - k_{rn}^2} \text{ is imaginary} \\ \qquad\qquad \Rightarrow \text{Evanescent mode} \end{cases} \tag{5}$$

The zeroth mode wave ($n = 0$ and $\alpha_{r0} = 0$) is:

$$P_0 = \varphi_0 \exp(ikx - iwt) \tag{6}$$

which is the classical one-dimensional (1-D) WH solution and is referred to as M0 hereafter. The first radial mode ($n = 1$ and $\alpha_{r1} = 3.8317$), hereafter referred to as M1, is excited if:

$$k^2 \geq k_{r1}^2 \Rightarrow \frac{w}{a} \geq k_{r1} = \frac{\alpha_{r1}}{R} \approx \frac{3.83}{R} \Rightarrow \frac{wR}{a} \geq 3.83 \tag{7}$$

From Eq. (7), the cut-off frequency (Rienstra & Hirschberg, 2004) beyond which the classical one dimensional WH theory is no longer valid is:

$$f > f_1 = \frac{\alpha_{r1}}{\pi}\frac{a}{D} \approx \frac{3.83}{\pi}\frac{a}{D} \tag{8}$$

For a later discussion, the cut-off frequency beyond which the second mode (M2) is excited is:

$$f > f_2 = \frac{\alpha_{r2}}{\pi}\frac{a}{D} \approx \frac{7.01}{\pi}\frac{a}{D} \tag{9}$$

From Eqs (3) and (4), the phase velocity υ_n can be determined from the phase of the solution in Eq. (4) as follows:

$$\upsilon_n = \frac{w}{k_{xn}} = \frac{w}{\sqrt{(w/a)^2 - k_{rn}^2}} \geq a \tag{10}$$

and the group velocity V_{gn} of the nth mode is:

$$V_{gn} = \frac{\mathrm{d}w}{\mathrm{d}k_{xn}} = \frac{\mathrm{d}\left[a\sqrt{k_{xn}^2 + k_{rn}^2}\right]}{\mathrm{d}k_{xn}} = \frac{ak_{xn}}{\sqrt{k_{xn}^2 + k_{rn}^2}} = \frac{a\sqrt{(w/a)^2 - k_{rn}^2}}{(w/a)} = \frac{a^2}{\upsilon_n} \leq a \tag{11}$$

Figure 1 plots group velocity Eq. (11) for the first four modes and shows that waves at frequencies close to the cut-off frequencies propagate at very low speed. Figure 1 aids later discussions.

The total energy per unit wavelength λ_n in the nth mode is (Rienstra & Hirschberg, 2004):

$$E_n = \frac{1}{\lambda_n}\int_0^{2\pi}\int_0^R\int_0^{\lambda_n} \frac{1}{2}\left(\rho V_{xn}^2 + \rho V_{rn}^2 + \frac{P_n^2}{\rho a^2}\right) r\,\mathrm{d}r\,\mathrm{d}x\,\mathrm{d}\theta = \frac{\varphi_n^2 \pi R^2}{2\rho a^2} J_0^2(\alpha_{rn}) \tag{12}$$

and the energy flux (i.e. power) is:

$$E_{Fn} = \frac{1}{t_p}\int_0^{2\pi}\int_0^R\int_0^{t_p} (P_n V_{xn}) r\,\mathrm{d}r\,\mathrm{d}\theta\,\mathrm{d}t = \underbrace{\frac{\varphi_n^2 \pi R^2}{2\rho a^2} J_0^2(\alpha_{rn})}_{E_n} \underbrace{a^2 \frac{k_{xn}}{w}}_{V_{gn}} = E_n V_{gn} \tag{13}$$

where $t_p = 2\pi/w$. For $n > 0$, Eq. (11) and Fig. 1 reveal that

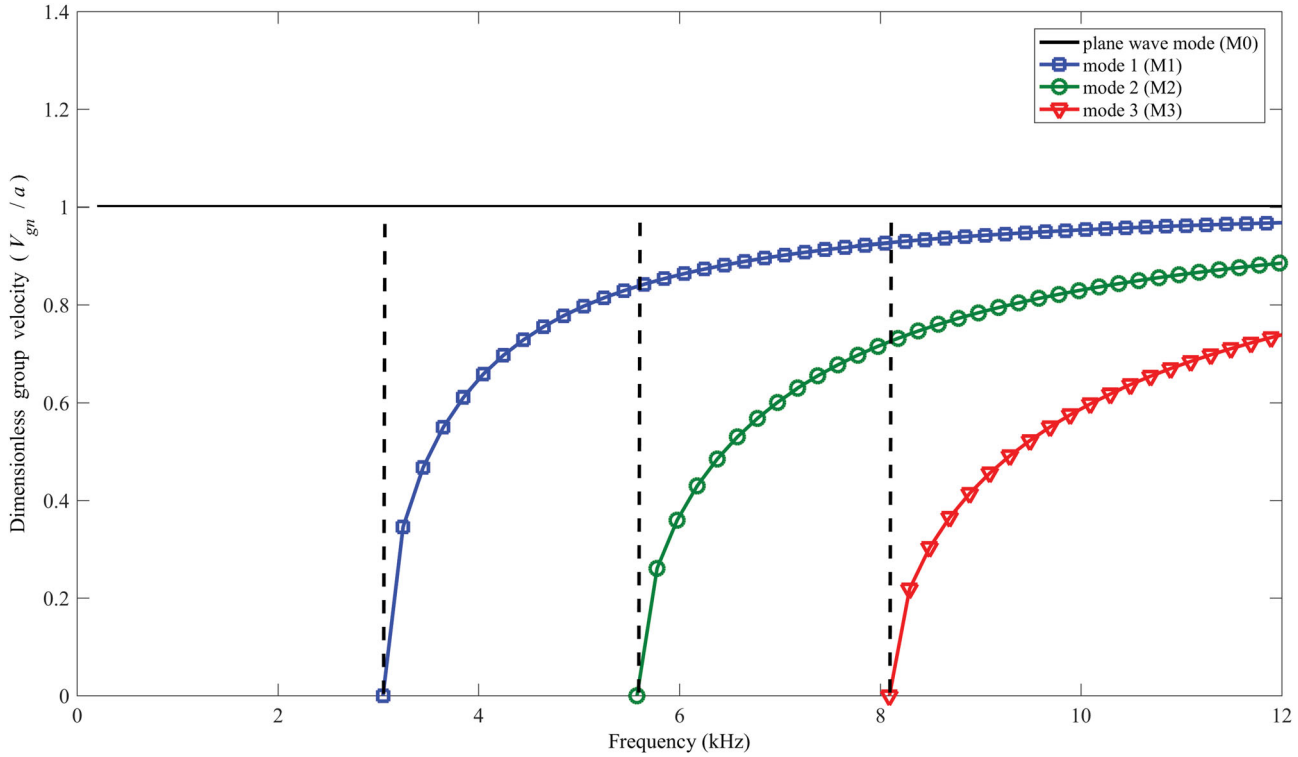

Figure 1 Group velocity for the first four modes

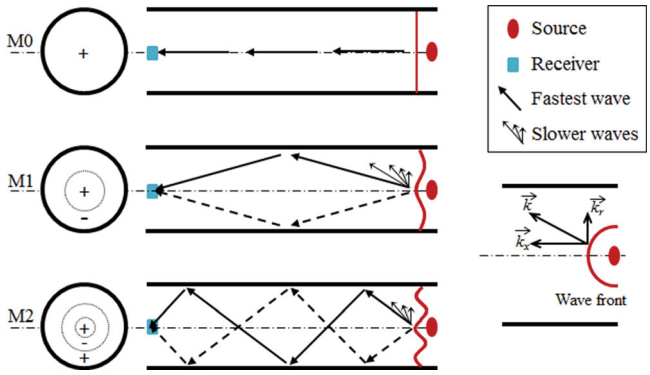

Figure 2 A descriptive sketch of multi-path effect (zigzag-type of path) in axisymmetric pipe flow

the group velocity is smaller than the WH wave speed a. The fact that energy propagates at a speed slower than a is due to the fact that modes with $n > 0$ do not travel parallel to the pipe axis; instead, they take a zigzag-type path (Rienstra & Hirschberg, 2004). Figure 2 provides a sketch of the path of different wave modes where the direction wave travel is dictated by the following wave number vector relation:

$$\vec{k} = k_{rn}\vec{i} + k_{xn}\vec{j} \tag{14}$$

where $\vec{i}$ and $\vec{j}$ are unit vectors along the r and x directions, respectively. The speed along each path is given by the phase velocity (Eq. (10)), which shows that higher wave modes travel faster but take longer paths. The zigzag path type is dictated from Eq. (14) where the direction of the wave is normal to the wave front (Fig. 2). The high-frequency waves will propagate along a diagonal direction with a certain angle (θ_{kn}) from the pipe centreline when $k_{rn} \neq 0$ in Eq. (14). Only M0 waves travel in straight paths along the pipe for which $k_{r0} = 0$ in Eq. (14). The fact that different wave modes take different paths is referred to as the multi-path process and is the primary reason that high-frequency waves are dispersive. The angle of propagation θ_{kn} is defined as follows:

$$\theta_{kn} = \begin{cases} \tan^{-1}\left(\dfrac{k_{rn}}{k_{xn}}\right) = \tan^{-1}\left(\dfrac{k_{rn}}{\sqrt{(w/a)^2 - k_{rn}^2}}\right) \\ \text{or} \\ \cos^{-1}\left(\dfrac{k_{xn}}{k}\right) = \cos^{-1}\left(\dfrac{ak_{xn}}{w}\right) \end{cases} \tag{15}$$

and its variation with frequency for the first three higher modes is given in Fig. 3. Figure 3 shows that, at the cut-off frequencies, θ_{kn} is 90° (i.e. at a cut-off frequency a wave propagates radially, not axially). Therefore, waves at cut-off frequencies are standing waves and do not propagate along the pipe. For waves propagating at frequencies near (but not at) the cut-off frequencies, their angle of propagation is slightly less than 90°; hence, they propagate along the pipe but take a (much) longer path. On the other hand, Fig. 3 shows that the farther away the wave frequency is from the cut-off, the smaller is its angle of propagation. Therefore, the smaller is the angle, the shorter is the path taken by the wave, and the faster is its speed of propagation.

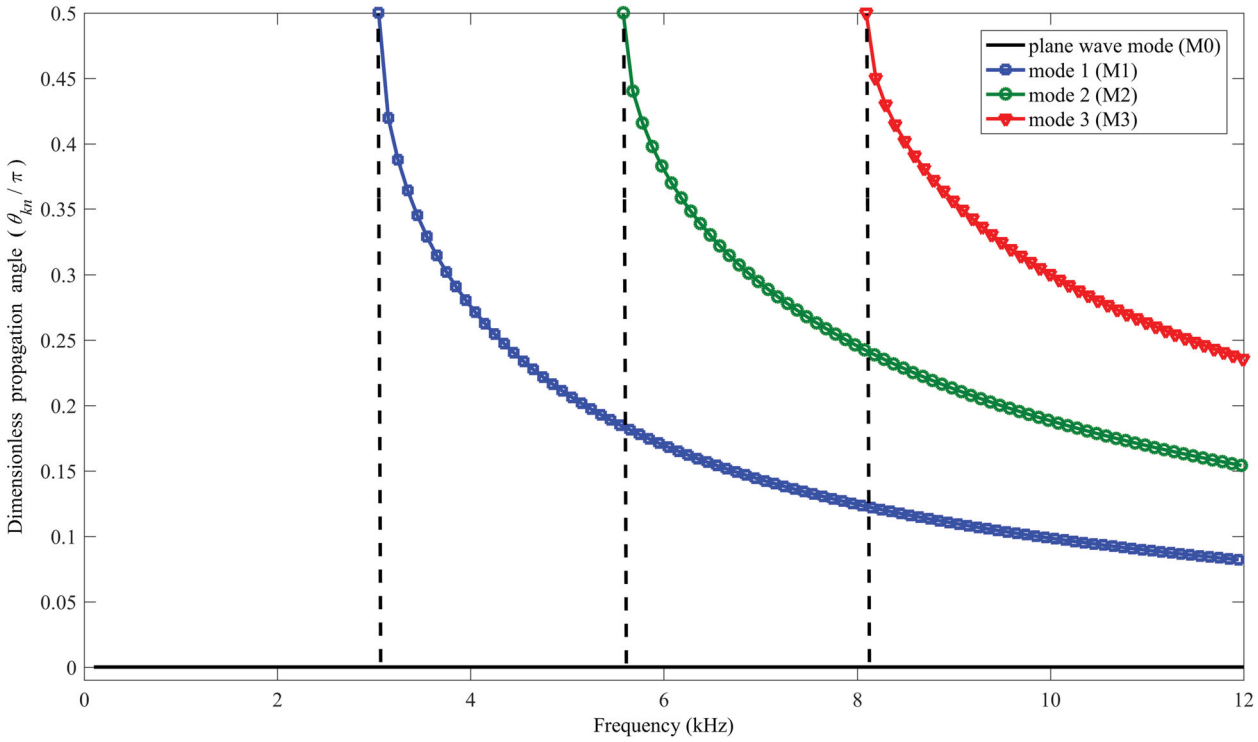

Figure 3 Variation in propagation angle (Eq. (15)) with frequency for the first three higher modes

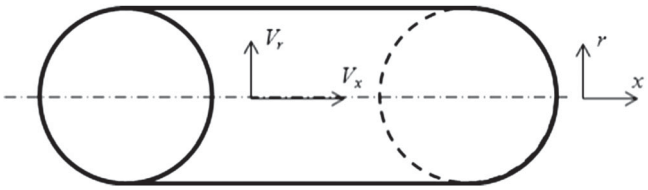

Figure 4 A sketch of a pipe and the coordinate system

3 Governing equation

Let V_x and V_r denote the macroscopic velocity components in x- and r-directions (Fig. 4), respectively; and ρ, and P denote the fluid density and the pressure, respectively. The 2-D axisymmetric continuity and Navier–Stokes equations for a compressible fluid in cylindrical coordinates are (Ghidaoui, 2004):

$$\frac{\partial \boldsymbol{U}}{\partial t} + \frac{\partial \boldsymbol{F}}{\partial r} + \frac{\partial \boldsymbol{G}}{\partial x} = \boldsymbol{S} \tag{16}$$

$$\boldsymbol{U} = \begin{pmatrix} \rho \\ \rho V_r \\ \rho V_x \end{pmatrix};\ \boldsymbol{F} = \begin{pmatrix} \rho V_r \\ \rho V_r^2 + P \\ \rho V_r V_x \end{pmatrix};\ \boldsymbol{G} = \begin{pmatrix} \rho V_x \\ \rho V_r V_x \\ \rho V_x^2 + P \end{pmatrix} \tag{17}$$

$$\boldsymbol{S} = \begin{pmatrix} -\rho V_r / r \\ -\rho V_r^2 / r \\ -\rho V_r V_x / r \end{pmatrix} \tag{18}$$

The terms in Eq. (18) are due to the cylindrical coordinate formulation. The state equation relating the pressure to the fluid density is:

$$\frac{\partial P}{\partial \rho} = \frac{K}{\rho} \tag{19}$$

where K is the bulk modulus and ρ is the density. Equation (19) is for a rigid pipe. If the fluid is water, and the pipe is perfectly rigid, the wave speed a is about 1440 m s^{-1}. Equation (19) can also be applied to slightly deformable pipes, where an effective bulk modulus of elasticity, which depends on pipe thickness, diameter, and Young's modulus of elasticity, is used. For simplicity of calculation in this paper, a is taken to be 1000 m s^{-1}.

4 Proposed numerical solution for the system of Eqs (16)–(18)

In this paper, the behaviour of high-frequency waves in a fluid-filled pipe is studied numerically. In a finite volume (FV) discretized numerical domain, these high-frequency waves lead to severe discontinuities at the cell interface. As a result, such waves require subtle techniques to faithfully represent the physical characteristics of the propagating waves and to avoid numerical anomalies such as dispersion and high dissipation rate (Ohwada, Adachi, Xu, & Luo, 2013). Since high-frequency waves are dispersive (Eqs (10) and (11)), their physical dispersion requires high precision in the numerical results; and to control errors numerical dispersion must be minimized. For this reason, finite difference methods (such as Lax–Wendroff schemes) are avoided due to their dispersive behaviour (Hirsch, 2007), and instead, a FV shock-capturing scheme is used. The

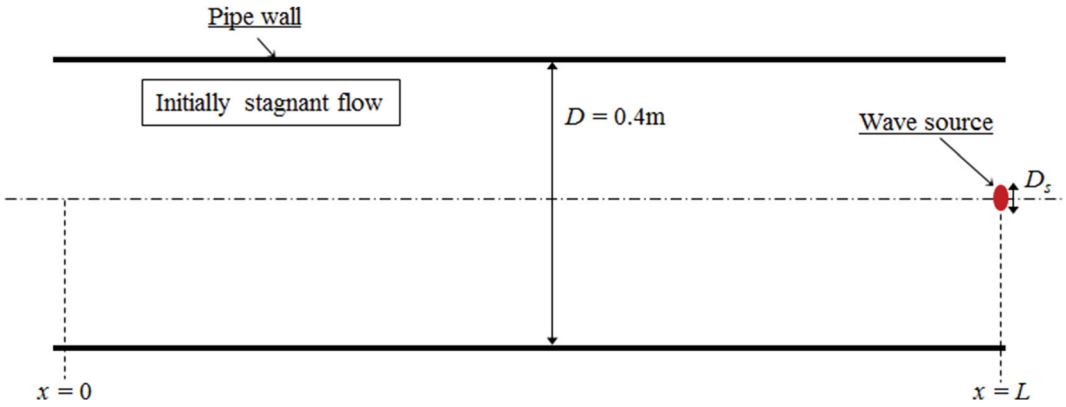

Figure 5 A sketch of the numerical pipe set-up

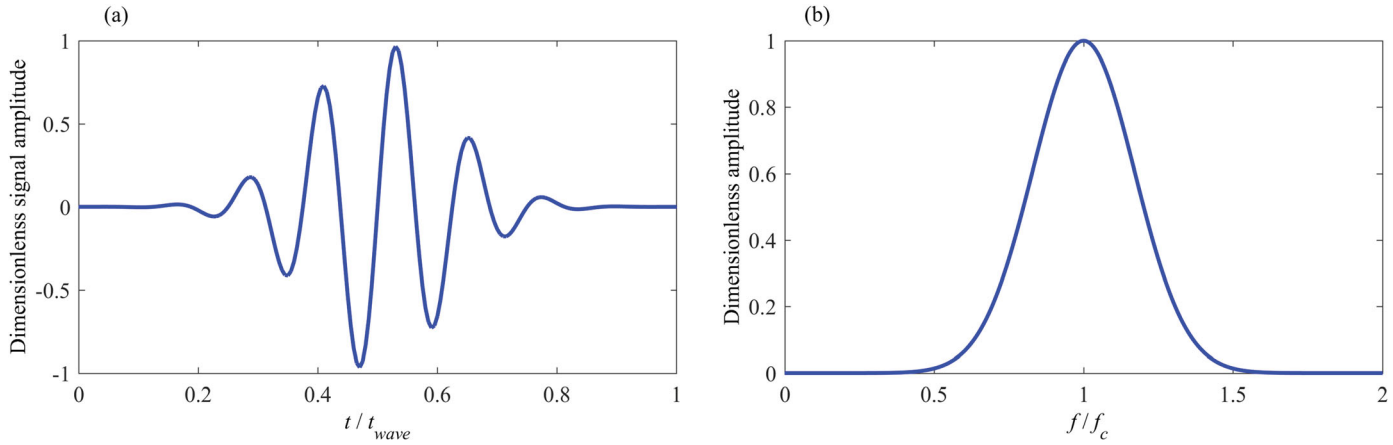

Figure 6 Source waveform. (a) time domain variation; (b) frequency domain variation

numerical dissipation mechanism of FV Godunov-type schemes is complex and depends on the grid resolution, flux evolution and the projection stage (Xu & Li, 2001). In order to minimize numerical dissipation and, at the same time, achieve an acceptably rapid convergence, higher order accuracy is required. For the current work, a fifth order two-dimensional (2-D) FV numerical scheme based on the Riemann solver (Toro, 2009) is developed and used. The fifth order accuracy is achieved by using a weighted essentially non-oscillatory (WENO) reconstruction (Jiang & Shu, 1996). Details of the developed schemes can be found in Louati (2016).

4.1 *Numerical and physical parameters and initial and boundary conditions*

The simple numerical system being modelled comprises a pipe with diameter $D = 0.4\,\text{m}$ and length L (Fig. 5). Flow is considered inviscid and initially stagnant. The wave form at the source is given in Fig. 6. The wave is generated at $x = L$ and its mathematical form is:

$$\begin{cases} P_F(t) = P_s \exp\left(-2\dfrac{{w_c}^2}{\beta^2}\log(10)\left(t-\dfrac{\beta}{w_c}\right)^2\right)\sin\left(w_c\left(t-\dfrac{\beta}{w_c}\right)\right) \\ \text{where} \quad 0 < t \le t_{wave} = \dfrac{\beta}{w_c} \text{ with } \beta = 16\pi; 0 \le r \le \frac{D_s}{2} \end{cases} \tag{20}$$

where $w_c = 2\pi f_c$ is the angular central frequency (in rad s^{-1}) with f_c the central frequency (in Hz); P_F is the transient pressure at the source; $P_s = 0.1P_0$ is the maximum transient pressure at the source with P_0 the initial pressure in the pipe; t_{wave} is the duration of the wave generated at the source; and β is a coefficient that controls the frequency bandwidth (FBW); D_s is the source diameter (Fig. 5). The source is circular in shape with diameter D_s and is located at the pipe centreline ($r = 0$) at $x = L$ (Fig. 5). The wave form given by Eq. (20) allows the modeller to select a desired FBW. For example, Fig. 6 shows an input signal that has a FBW of [$0.5f_c$ to $1.5f_c$].

Since the pipe system is assumed to be axisymmetric, the numerical domain is a rectangular region that extends from $r = 0$ to $r = R$ and from $x = 0$ to $x = L$. The boundary conditions at $r = 0$ and $r = R$ are:

$$\left.\frac{\partial P}{\partial r}\right|_{r=0} = 0; \quad V_r|_{r=0} = 0; \quad \left.\frac{\partial V_x}{\partial r}\right|_{r=0} = 0 \tag{21}$$

and

$$\left.\frac{\partial P}{\partial r}\right|_{r=R} = 0; \quad V_r|_{r=R} = 0; \quad \left.\frac{\partial V_x}{\partial r}\right|_{r=R} = 0 \tag{22}$$

A Taylor series expansion is used to discretize the above boundary conditions and ghost cells are employed at the boundaries.

At $x = 0$ and at $x = L$ a non-reflective boundary condition is used, and Eq. (20) is imposed. The non-reflective boundaries are modelled using the characteristic boundary condition (Thompson, 1987; Thompson, 1990). Note that numerical reflections are thus minimized but cannot be eliminated completely (Louati, 2016; Richards, Zhang, Chen, & Nelson, 2004). Therefore, the pipe length for all test cases is selected to be long enough so that the domain of interest is not contaminated by artificial reflections during the duration of the simulation.

Based on a non-parallelized algorithm, the considered grid mesh is $N_R \times N_X = 20 \times 5000$, which results in a CPU time of about 12 h for $L = 50$ m and with wave whose central frequency $f_c = 4000$ Hz. For the case $f_c = 6800$ Hz (used in Section 5.2), a finer mesh of $N_R \times N_X = 40 \times 10{,}000$ is required and the CPU time is about 51 h.

5 Results and discussion

5.1 *High-frequency wave behaviour under resonating source*

In this section, the FBW is chosen to include the cut-off frequencies of excited higher modes. In this way, the resonant response is studied, and the results could be compared to the properties of the 2-D inviscid wave theory (Section 2) where the natural cut-off frequencies are well defined. While the analytical solution is for the homogeneous case, the numerical solution is forced with a pressure source described by Eq. (20). Therefore, the eigenvalues and their associated features such as wave path, dispersion, cut-off and cut-on modes can be compared, but pressure and velocity amplitudes cannot.

5.1.1 *Dispersion and behaviour of higher wave modes*

Three tests are conducted using three different central frequencies $f_c = 1000$ Hz, 3000 Hz and 5000 Hz and using a source diameter $D_s = 0.1D$. The upper bound frequency content (UBFC) in these three test cases is 1500 Hz, 4500 Hz and 7500 Hz, respectively. Results are given in Figs 7 and 8. Figures 7a and 8a are for a frequency range of 500–1500 Hz, Figs 7b and 8b are for a frequency range of 1500–4500 Hz, and Figs 7c and 8c are for a frequency range of 2500–7500 Hz. These figures show both time and frequency domain plots of the pressure at $x = L - 7\,\text{m} = 3$ m (i.e. 7 m from the wave source) and $x = L - R/2\,\text{m} = 9.9$ m (i.e. 0.1 m from the wave source) along the pipe centreline. The dashed lines in Fig. 8 indicate the position of the relevant cut-off frequencies. According to Eq. (8) and Fig. 1, if the frequency is higher than $f_1 = 3050$ Hz, the first higher mode (M1) is excited and the classical 1-D WH theory is no longer valid. This is in good agreement with the numerical tests in Figs 7 and 8. The signals with $f_c = 3000$ Hz and $f_c = 5000$ Hz are dispersive and do not conform to the classical 1-D WH theory as the wave form of the signal is distorted due to the dispersion of the signal (Fig. 7b and 7c). On the other hand, the signal with $f_c = 1000$ Hz (Figs 7a and 8a) is non-dispersive and behaves according to the classical 1-D WH

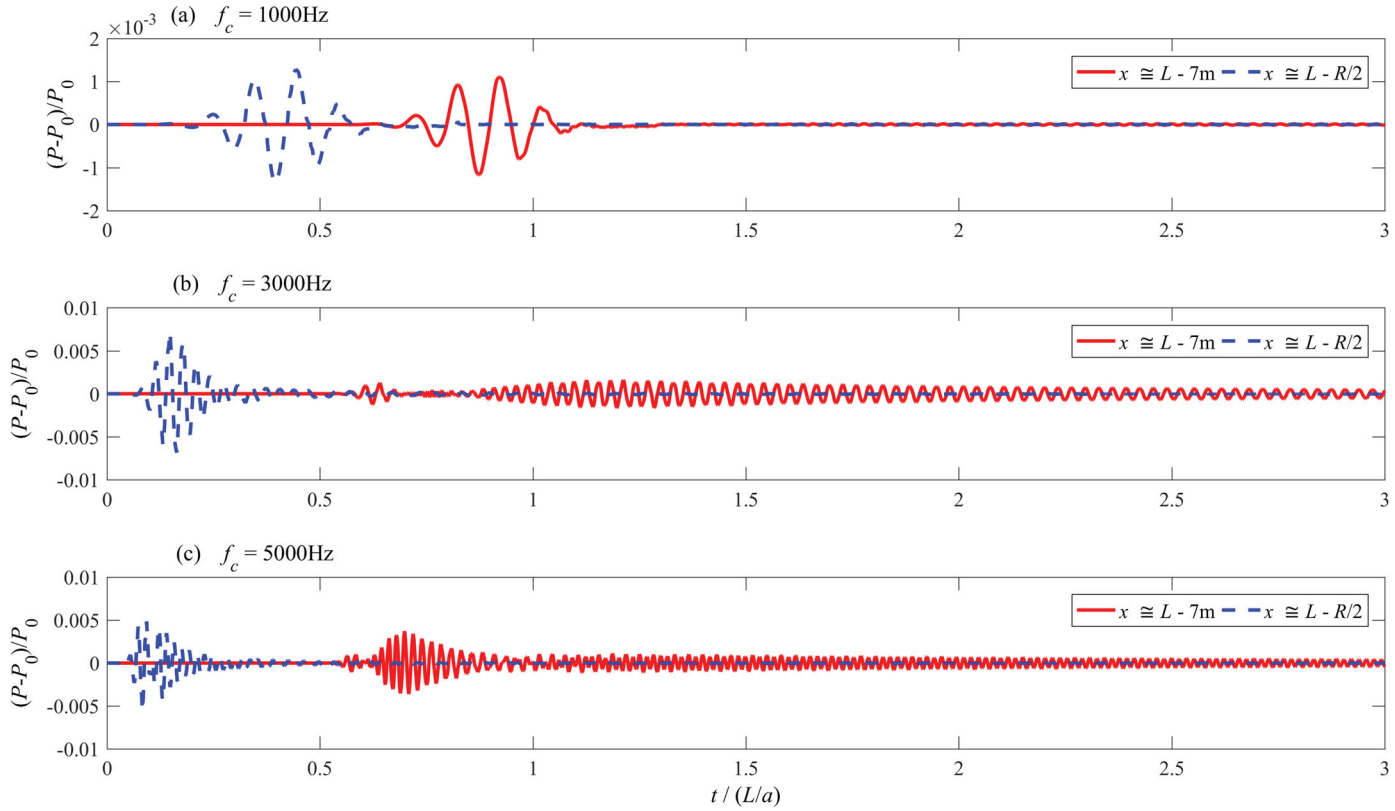

Figure 7 Dimensionless pressure variation with time measured near the source and at 7 m away from the source. (a) $f_c = 1000$ Hz; (b) $f_c = 3000$ Hz, (c) $f_c = 5000$ Hz. For all cases $D_s = 0.1\ D$, $r \approx 0$ and $L = 10$ m

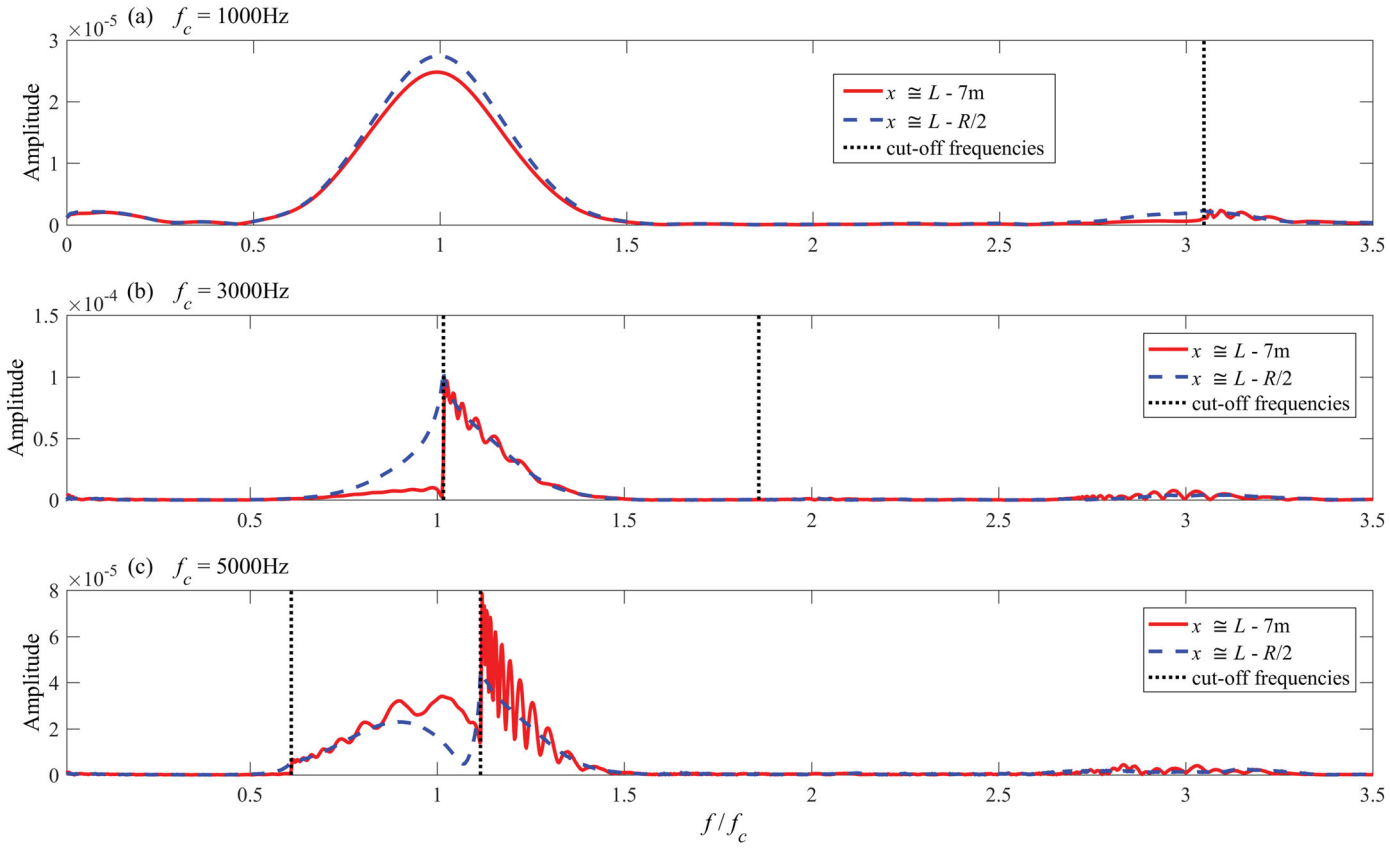

Figure 8 Dimensionless amplitude in the frequency domain corresponding to the pressure signals in Fig. 7 measured near the source and at 7 m away from the source. (a) $f_c = 1000$ Hz; (b) $f_c = 3000$ Hz, (c) $f_c = 5000$ Hz. For all cases $D_s = 0.1D$ and $r \approx 0$

theory. The frequency axis in Fig. 8a is extended to show that no higher modes are excited. Figure 8b ($f_c = 3000$ Hz) shows that both M0 and M1 are excited, which agrees with Eq. (8). In Fig. 8c ($f_c = 5000$ Hz), the second mode (M2) is also excited as predicted from Eq. (9).

The dispersion of the waves along the pipe is associated with radial waves. Therefore, it is important to analyse the behaviour of these radial waves. Figure 9 shows the surface plot (along r and x) of the pressure waves for the three tests (i.e. $f_c = 1000$ Hz, 3000 Hz and 5000 Hz). The pressures are sampled at $t = t_{wave} = 8/f_c$, $t = 0.66L/a$ and $t = 0.9L/a$ (Fig. 9). The study domain in this case is of length $L = 50$ m. For the case with $f_c = 1000$ Hz (UBFC = 1500 Hz $< f_1 = 3050$ Hz), the classical 1-D WH theory holds (Fig. 9a, 9d and 9g). However, for the case where $f_c = 3000$ Hz (Fig. 9b, 9e and 9h), both M0 and M1 are excited, but the amplitude of M0 is much smaller than M1. For the case with $f_c = 5000$ Hz, M0, M1 and M2 are excited as can be seen from Figs 9c, 9f, 9i and 10. For better visualization, an enlarged version of Fig. 9i is given in Fig. 10. The region occupied by M2 is indicated in Fig. 10. It is clear that M2 propagates at slower speed than the two other modes as it is lagging behind M1 and M0 which is as expected from Eq. (11) and Fig. 1, confirming that the speed at which M2 propagates is slower. In addition, it is seen that M1 spreads over a longer region for the case with $f_c = 5000$ Hz (Fig. 9i) than for the case with $f_c = 3000$ Hz (Fig. 9f). The wave source with $f_c = 5000$ Hz excites M1 waves in the range 3050–7500 Hz. The speed of energy of the M1 excited modes in this case ranges from 0 to 913 m s^{-1} (Fig. 1). The wave source with $f_c = 3000$ Hz excites M1 waves in the range 3050–4500 Hz. The speed of energy propagation of the M1 excited modes in this case ranges from 0 to 735 m s^{-1}. The computed results in Fig. 9h ($f_c = 3000$ Hz) show that the leading M1 wave propagates at a speed of $0.65/(0.9/a) \approx 722$ m s^{-1}. On the other hand, the computed results plotted in Fig. 9i ($f_c = 5000$ Hz) indicate that the leading M1 wave travels at $0.81/(0.9/a) \approx 900$ m s^{-1}. Both speeds agree well with the theoretical speeds in Fig. 1. The differences between computed and theoretical values are likely due to the fact that the leading M1 waves carry little energy and therefore do not appear clearly in Fig. 9h and 9i. This agreement in energy propagation speed at all excited frequencies is strong evidence that the numerical scheme has minimal dispersion and dissipation errors – a conclusion that is important for the remaining analysis in this paper.

The analytical solution Eq. (2) shows that at any given x, the nth mode ($n = 1, 2, \ldots$) is given by a Bessel function of zero order. The nodes of nth mode are located at $J_0(k_{rn}r) = 0$. For example, M1 has one node at $k_{r1}r \approx 2.4048$ which gives $r \approx 0.627R$. In addition, M2 has two nodes: one at $r \approx 0.3427R$ and the other at $r \approx 0.787R$. These nodes are clearly shown in Fig. 10. Figure 10 shows that there is a region where the node of M1 is clear, which implies that M2, if it exists, is negligible

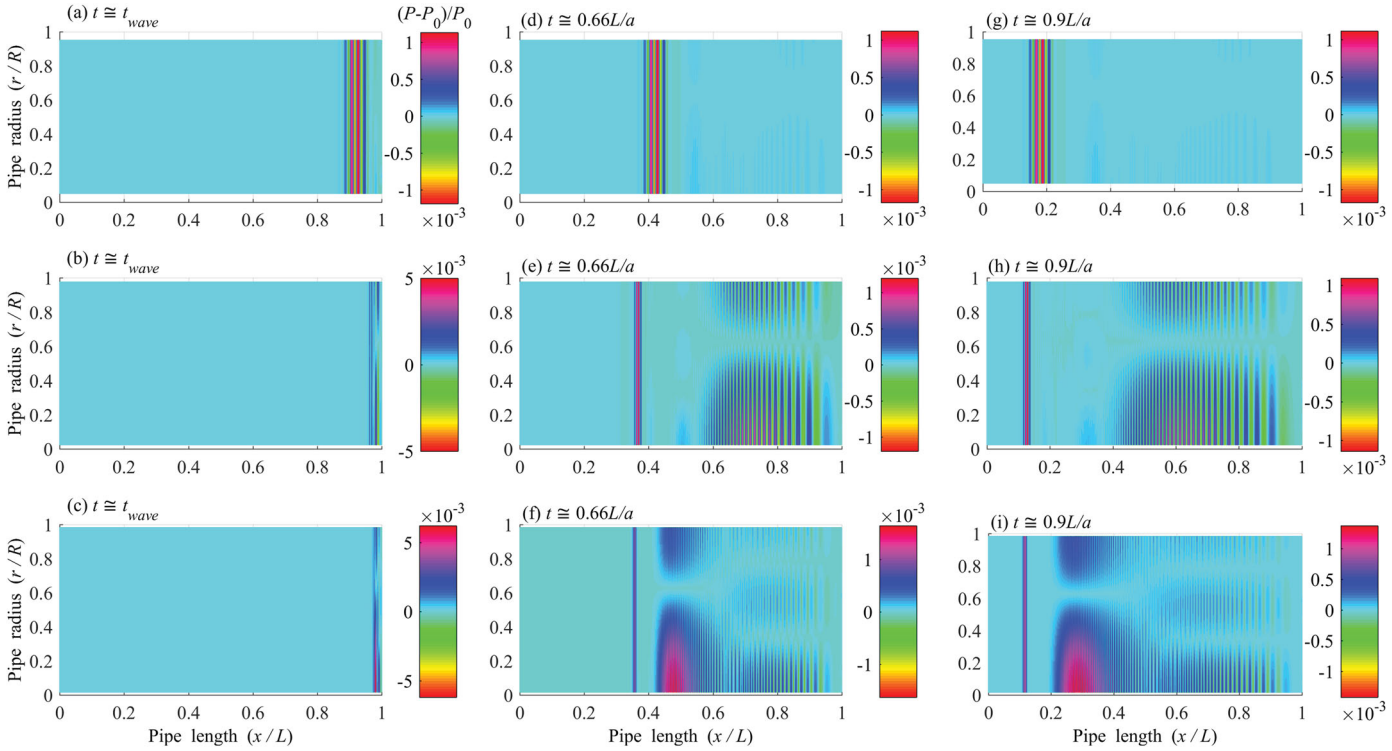

Figure 9 Dimensionless pressure variation (in colour) in the r–x space plane when different central frequencies are used: (a–c) $f_c = 1000$ Hz, (d–f) $f_c = 3000$ Hz and (g–i) $f_c = 5000$ Hz. For all cases $D_s = 0.1D$ and $L = 50$ m

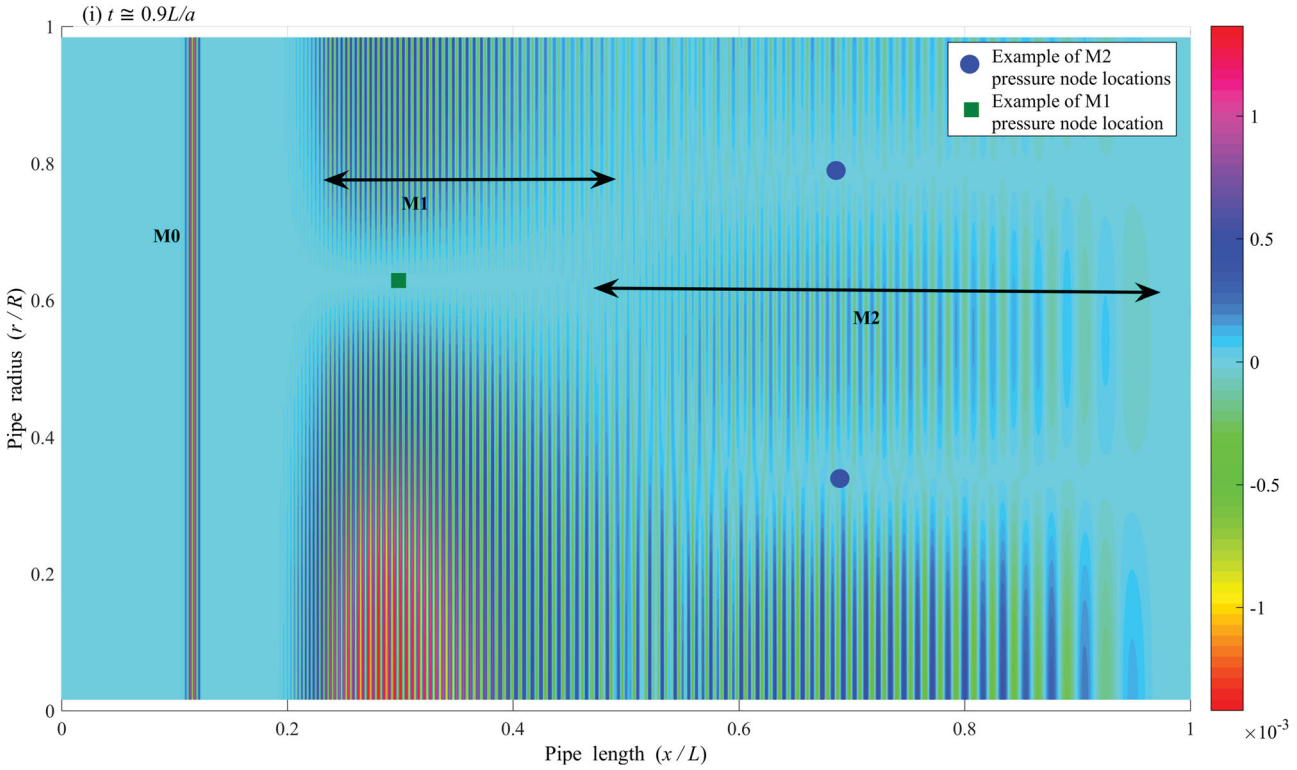

Figure 10 An enlarged portion of Fig. 9i for pressure distribution in the r–x space plane when $f_c = 5000$ Hz, $D_s = 0.1D$ and $t = 0.9L/a$ to show more detail of pressure nodes and mode forms

in this region. Conversely, there is a region where the nodes of M2 are clear, which implies that M1 is negligible in that region. Knowledge of the locations of these nodes could have important implications in locating sensors for TBDDM and/or for experimental investigation of the behaviour of high-frequency waves in pipes. For example, locating a sensor at the nodes of M1 means that the measured pressure would be dominated by noise. Knowing where to measure to maximize the signal

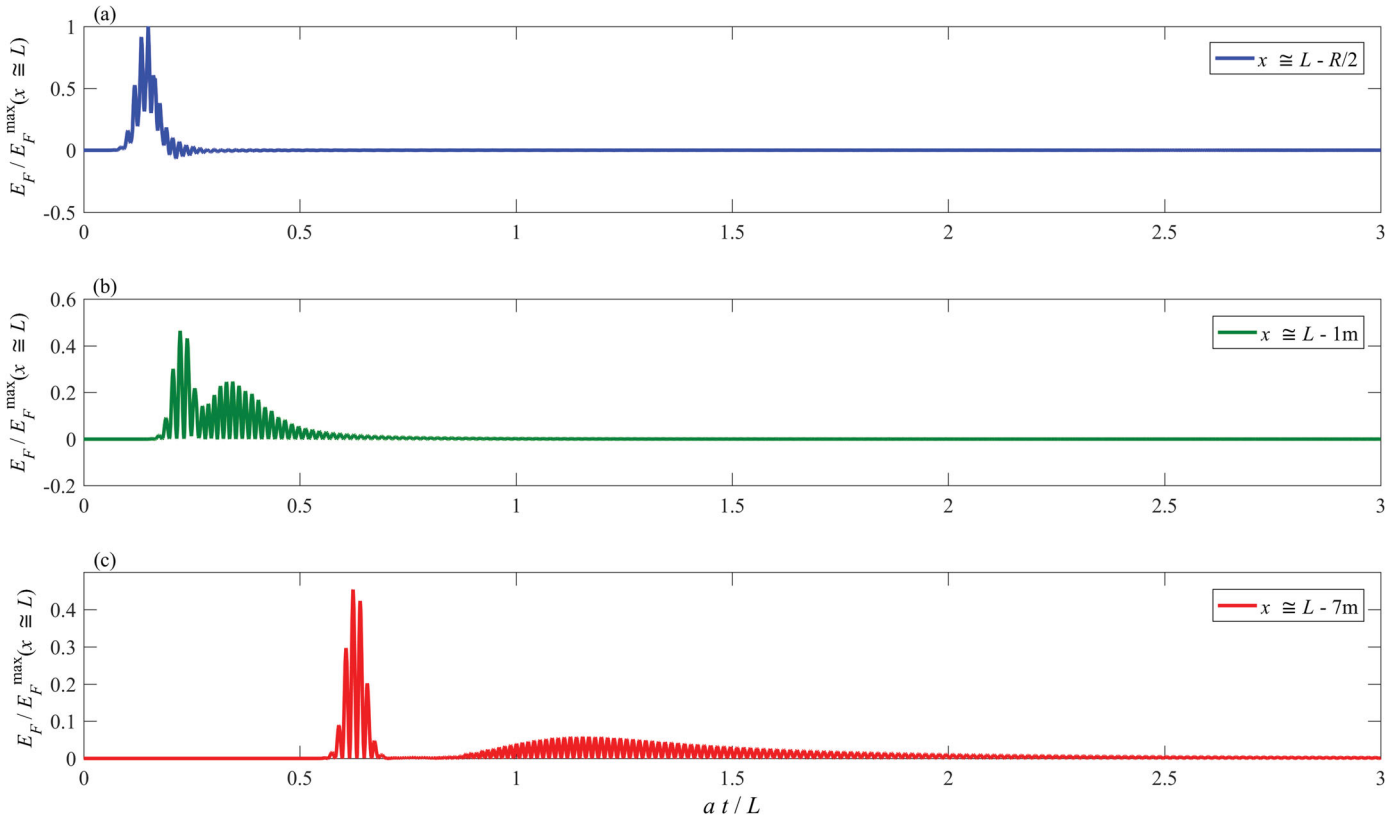

Figure 11 Energy flux computed numerically for the case of $f_c = 3000$ Hz and $D_s = 0.1D$ showing energy spread with distance from the source: (a) at $x = L - R/2$, (b) at $x = L - 1$ m and (c) at $x = L - 7$ m. For all cases $L = 10$ m (see Fig. 5)

strength is important in both research and any eventual field applications.

5.1.2 *Multi-path effect*

Figure 11 shows the energy flux (Eq. (13)) with time at three different locations along the pipe ($x \approx L - R/2$ m, $x \approx L - 1$ m and $x \approx L - 7$ m) where $f_c = 3000$ Hz, the FBW is [1500 Hz, 4500 Hz] and $D_s = 0.1D$. Waves with frequency in the range [1500 Hz, $f_1 = 3050$ Hz] are WH waves and propagate as M0 at the WH wave speed which is 1000 m s^{-1} (see Fig. 1). Frequencies in the range [$f_1 = 3050$ Hz, 4500 Hz] excite both M0 and M1 waves, where the group (energy) velocity of M0 is the same as the WH wave speed (Fig. 1) while that of the M1 varies continuously with frequency from 0 m s^{-1} to about 700 m s^{-1} (see Fig. 1). That is, the M0 wave leads the M1 for frequency in the range [$f_1 = 3050$ Hz, 4500 Hz]. The spatial separation between the fast propagating mode M0 and the slow propagating mode M1 is small near the wave source (Fig. 11a) and grows with distance from the source (Fig. 11b and 11c). In addition, due to variation with frequency in the propagation angle of M1 waves (Eq. (15) and Fig. 3) and group velocity (Fig. 1), these waves experience significant spatial spread with time (Fig. 11b and 11c). This spreading occurs because M0 travels parallel to the pipe axis while M1 waves travel along a zigzag (oblique) path (Fig. 2). This multi-path process results in wave dispersion. Such dispersion is absent in classical WH studies because only the axially propagating M0 mode is excited in those studies.

In practice, if one is to use HFW for defect detection by injecting these waves at one location and collecting pressure measurements at another location, it is important to know how the multi-path process and its associated dispersion influence the measurements. In addition, it is important to understand the wave dispersion process to ensure that it is not misconstrued as energy dissipation. Figure 11a shows that close to the source most of the energy is propagating as a coherent unit (Fig. 9d). However, in Fig. 11b and 11c, the energy exhibits temporal spread with a pronounced tail that grows longer and becomes more uniformly distributed as distance from the source increases. It is observed in Figs 1 and 3 that, for a given mode, the further away wave frequencies are from the cut-off frequency, the more uniform is the group velocity and the propagation angle. This uniformity in group velocity and propagation angle for certain ranges of frequencies means that the energy of these waves travels in a group down the pipe (Fig. 11b and 11c). However, over time the energy packet becomes spread over a longer distance. As a result, the amplitude of the packet is reduced and could eventually reduce to the same order as the noise or even lower.

Note that if the injected FBW contains a cut-off frequency, the speed at this frequency is zero, implying that the energy tail of the energy packet does not travel to the measurement station, which is located away from the source. A long measurement in time is needed to ensure that a significant portion of a wave packet passes the sampling location. Therefore, it is important to

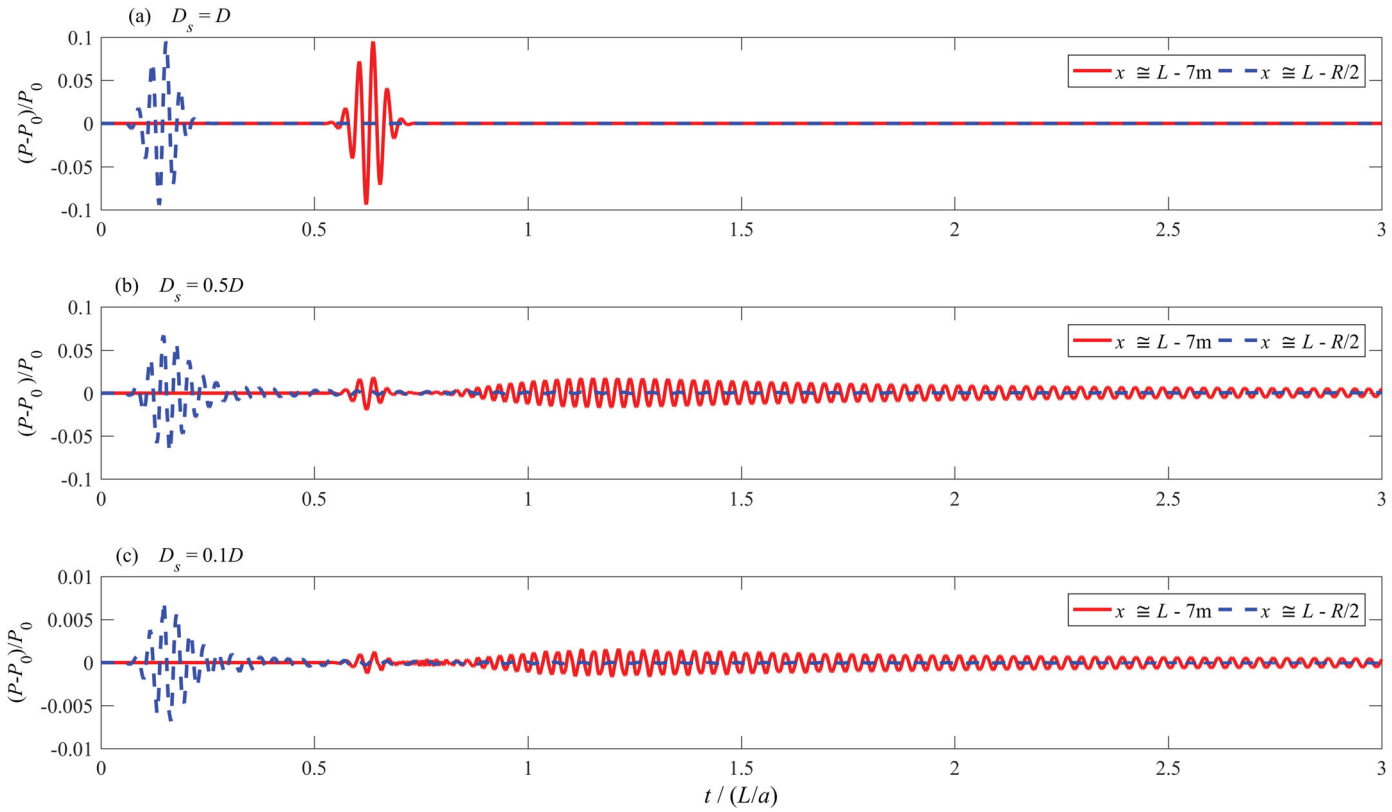

Figure 12 Dimensionless pressure variation with time measured near the source and at 7 m away from the source. (a): $D_s = D$; (b): $D_s = 0.5D$, (c): $D_s = 0.1D$. For all cases $f_c = 3000$ Hz, $r \approx 0$ and $L = 10$ m

take energy spread into account when conducting experiments by ensuring that measurements are taken (i) over a long enough time to ensure that the whole wave packet passes the sampling point; and (ii) close enough to the source to ensure they do not become "buried in the noise".

5.1.3 *Effect of transient source size*

In all previous test cases, the source diameter is fixed at $D_s = 0.1D$. In what follows, the effect of the source size on the wave dispersion behaviour is studied. This is an important consideration in the selection of a wave generator. In Figs 12 and 13, three tests are conducted using different source diameters, namely, $D_s = D$, $0.5D$ and $0.1D$. The central frequency is fixed to $f_c = 3000$ Hz. The total energy (potential and kinetic energy) along the pipe for these tests is given in Fig. 14. The results show that when $D_s = D$ (Figs 12a and 13a), the signal propagates as a plane wave (M0) despite the fact that the waves with frequencies in the range [$f_1 = 3050$ Hz, 4500 Hz] exceed the cut-off frequency f_1. The reason is that the wave generator, having the same diameter as the pipe, transmits signals that are independent of radius; thus, radial wave modes are not excited. However, if the M0 waves with frequencies higher than f_1 meet any non-uniformity in the pipe, the M1 mode becomes excited. For the cases where $D_s = 0.5D$ and $D_s = 0.1D$ (Figs 12b, 12c, 13b and 13c), the M1 mode is excited. In the $D_s = 0.5D$ case, more energy is carried by M0 (Fig. 14b) in comparison with the $D_s = 0.1D$ case (Fig. 14c). Therefore, the size of the radial scale of the wave source has a potentially significant influence on how the input energy is distributed over the different excited modes. Figure 14 shows that the smaller the source diameter, the less energy is carried by M0. In fact, as seen from Fig. 15a and 15b, which are magnified versions of Fig. 12b and 12c, the amplitude of M0 for the $D_s = 0.1D$ case (Fig. 15b) is about 10 times smaller than the amplitude for $D_s = 0.5D$ case (Fig 15a). The strong dependence of the amplitude of the M0 mode on the size of the wave source has important implications for TBDDM that are based on the plane wave assumption (e.g. Duan et al., 2013; Lee et al., 2013; Louati & Ghidaoui, 2015). If a wave source capable of generating high frequencies is used, and if the modeller develops a TBDDM based on the measurement on M0 waves alone, using a small diameter source seems not advisable because the amplitude of the M0 waves become negligibly small, making the signal to noise (or error) ratio small.

5.2 *Mode separation*

The FBW of the test cases studied so far in this paper include at least one cut-off frequency. This section considers a FBW that does not contain any cut-off frequency. The pipe diameter D and length L are 0.4 m and 100 m, respectively. The source has a cylindrical shape with diameter $D_s = 0.2$D located at the pipe

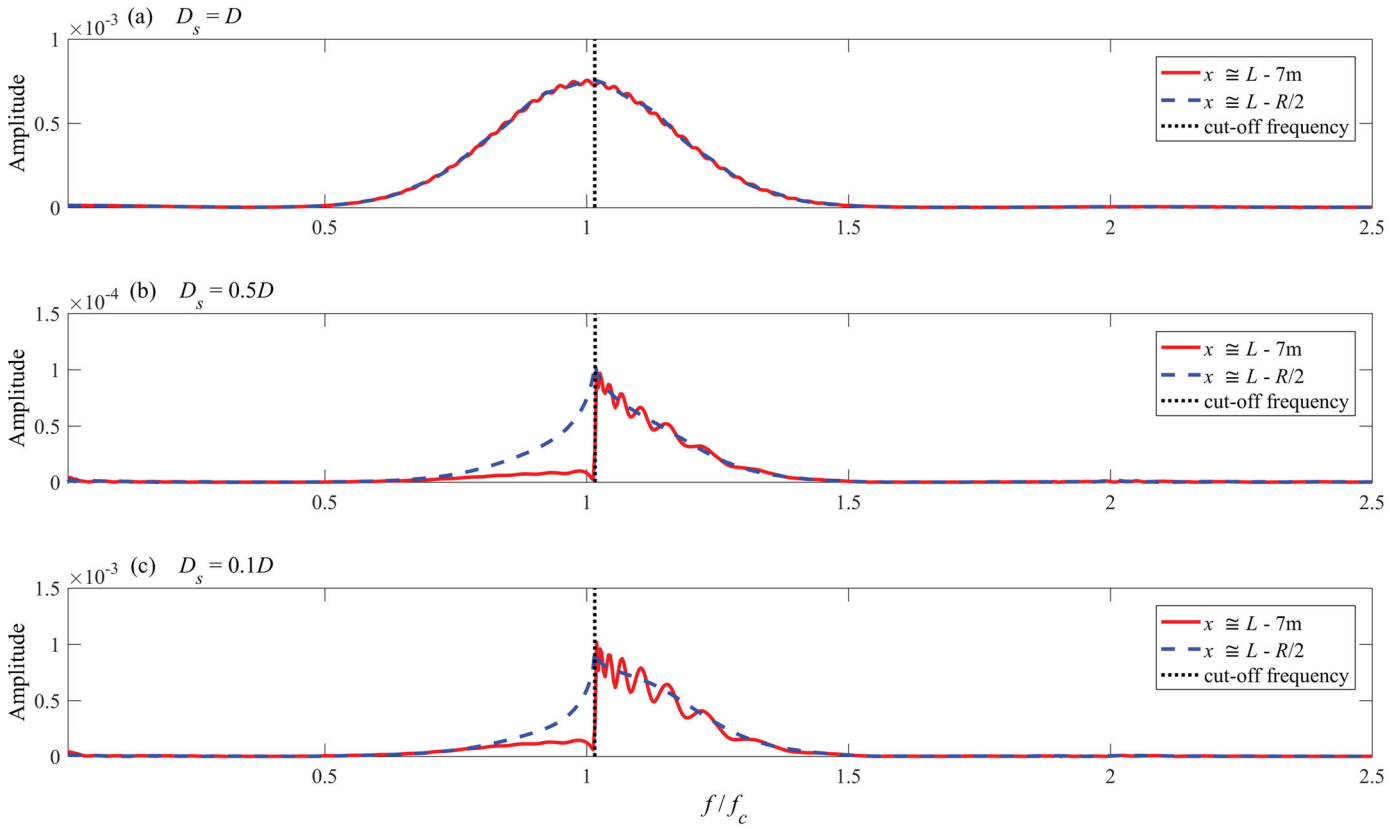

Figure 13 Dimensionless amplitude in the frequency domain corresponding to pressure signals in Fig. 12 measured near the source and at 7 m away from the source. (a) $D_s = D$; (b) $D_s = 0.5D$, (c) $D_s = 0.1D$. For all cases $f_c = 3000$ Hz, ($r \approx 0$) and $L = 10$ m

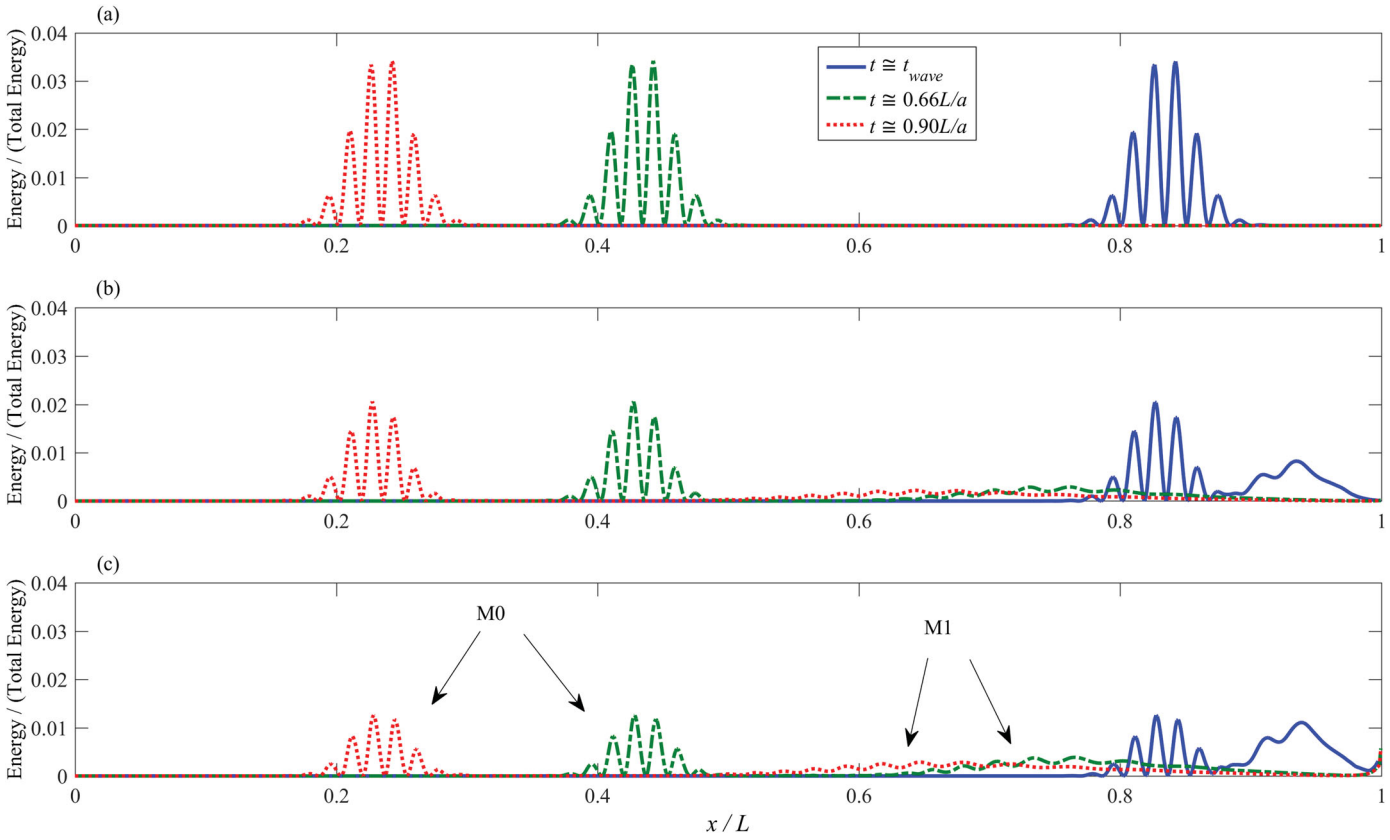

Figure 14 Dimensionless energy distribution along the pipe axis for different source size; (a) $D_s = D$, (b): $D_s = 0.5D$ and (c): $D_s = 0.1D$. For all cases $f_c = 3000$ Hz and $L = 10$ m

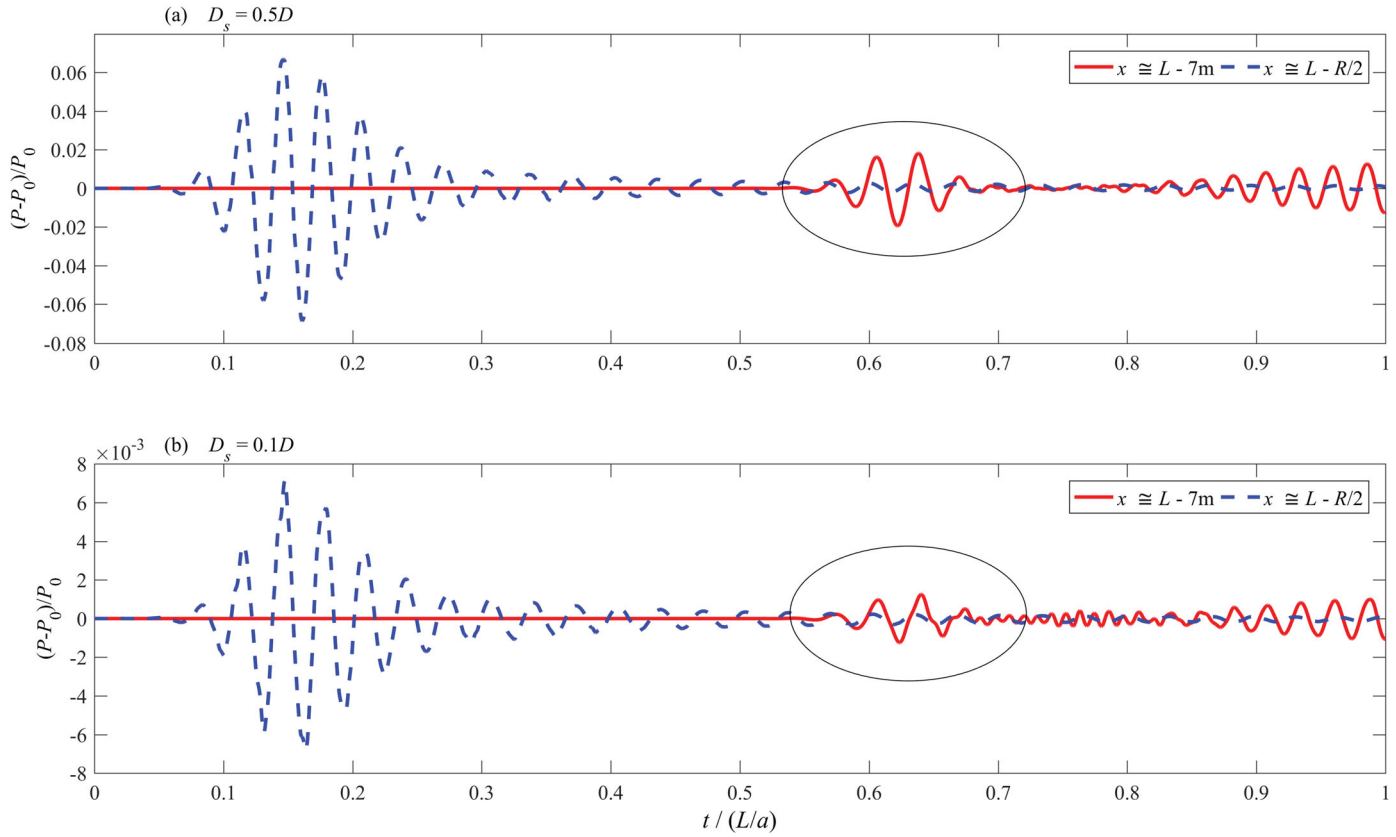

Figure 15 Magnified versions of Fig. 12b and 12c showing the separation of the plane mode (fundamental mode M0) from the higher mode about 7 m away from the source

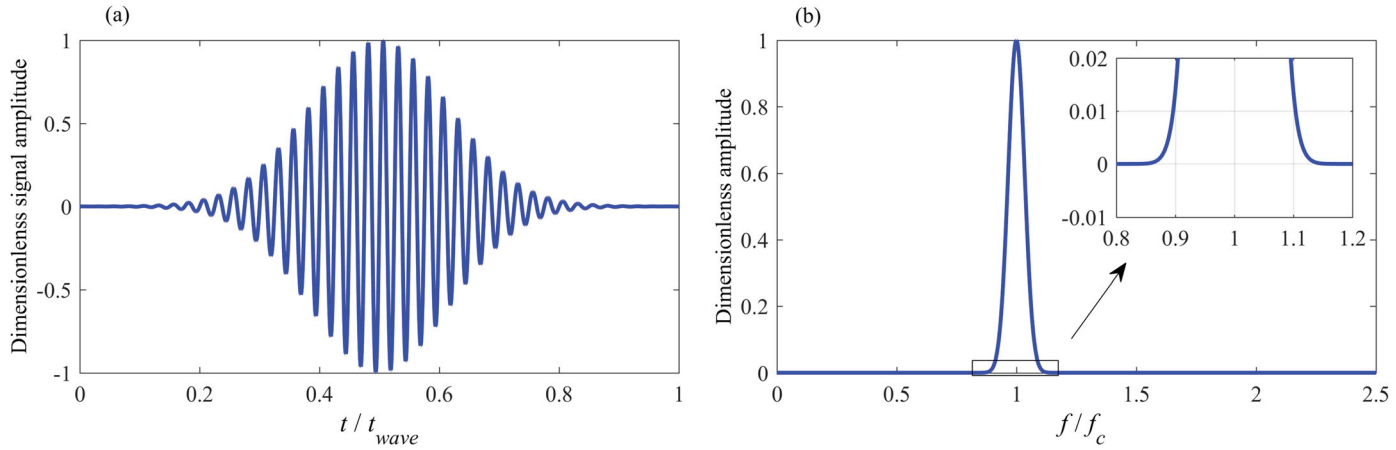

Figure 16 Input signal with narrow FBW: (a) time domain; (b) frequency domain

centreline ($r = 0$) and at $x = L$ (Fig. 5). Figure 16 shows the time and frequency domain response of the injected waveform where $\beta = 80\pi$ (see Eq. (20)) and shows that the FBW is within about [$0.9f_c$ to $1.1f_c$].

Figure 17 shows the pressure variation for $f_c = 6800$ Hz where M0, M1 and M2 are excited as expected from Fig. 1. The energy of higher mode waves travels at the group velocity (Fig. 1), which is bounded within the interval [$V_{gn}^{\min}$, $V_{gn}^{\max}$] where $V_{gn}^{\min}$ and $V_{gn}^{\max}$ are the minimum and maximum group velocity of the nth excited high mode and could be evaluated from Eq. (11). In particular, $V_{gn}^{\min}$ is evaluated by inserting the smallest value of the FBW into Eq. (11) and $V_{gn}^{\max}$ is evaluated by inserting the largest value of the FBW into Eq. (11).

From Eq. (11) and Fig. 1, M1 waves propagate at speeds within the interval [$V_{g_1}^{\min} \approx 865$ m s^{-1}, $V_{g_1}^{\max} \approx 910$ m s^{-1}] which are close to the plane wave speed (1000 m s^{-1}). On the other hand, M2 waves propagate at much lower speeds within the interval [$V_{g_2}^{\min} \approx 410$ m s^{-1}, $V_{g_2}^{\max} \approx 670$ m s^{-1}]. Therefore, although the different modes are injected simultaneously, they quickly become separated with the fastest mode (M0) leading, followed by M1, etc. Figure 17 illustrates this process for the case of M1 and M2 modes.

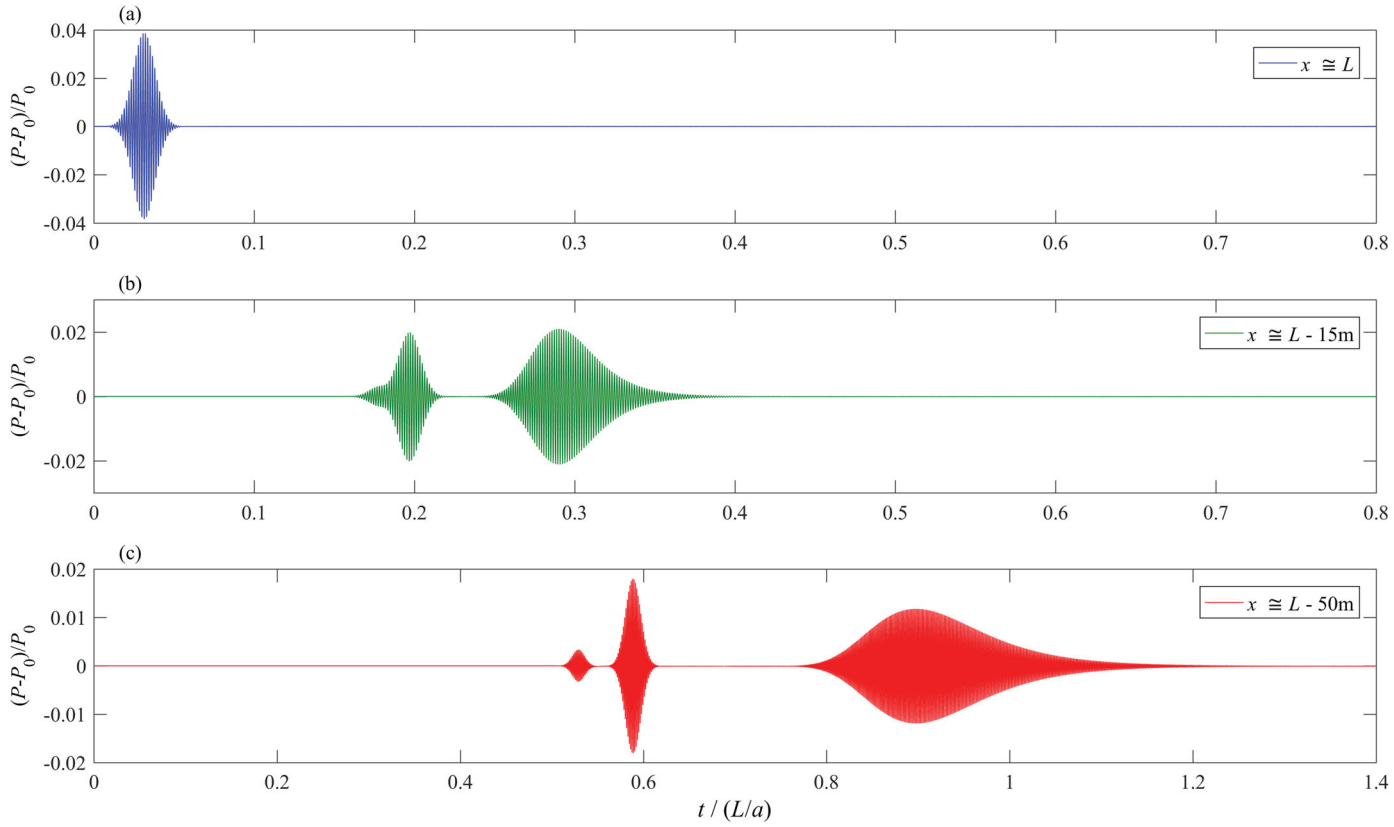

Figure 17 Variation of the pressure signal at the centreline with time for the case $f_c = 6800$ Hz where M0, M1 and M2 are excited: (a) at $x \approx L$ (near the source); (b) at 15 m away from the source; (c) at 50 m away from the source

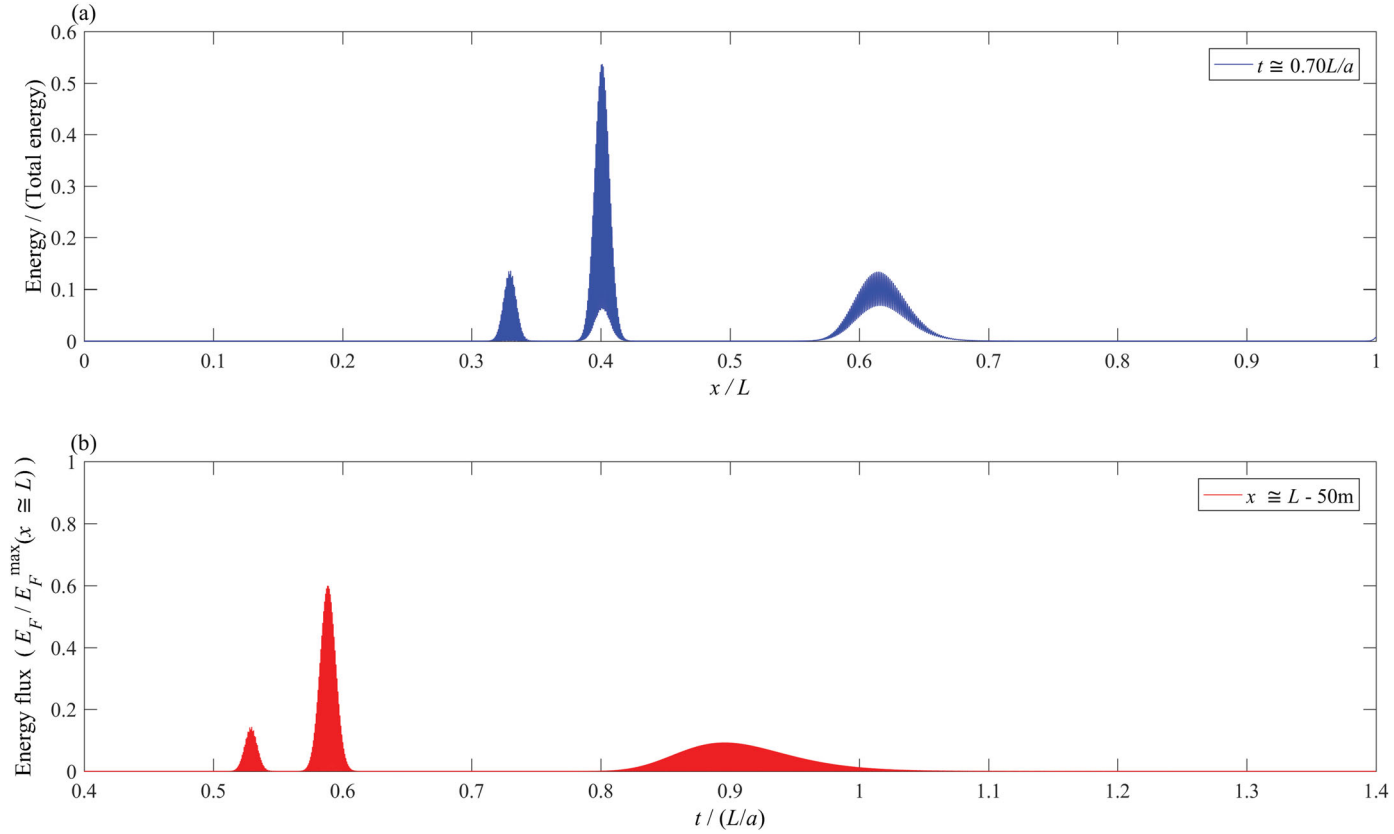

Figure 18 (a) Total area-averaged energy distribution along pipe at the time $t = 0.7L/a$; (b) Energy flux variation with time for the case of $f_c = 6800$ Hz measured at 50 m away from the source

The position at which the nth mode separates from mode $n-1$ can be estimated as follows:

$$\frac{x_n^s}{V_{g_n}^{\max}} = \left(\frac{x_n^s}{V_{g_{n-1}}^{\min}} + t_{wave}\right) \tag{23}$$

This equation provides the position x_n^s at which the fastest propagating wave of the nth mode is overtaken by the slowest propagating wave of the $(n-1)$th mode. Equation (23) can be re-written as:

$$x_n^s = \frac{t_{wave}}{((1/V_{g_n}^{\max}) - (1/V_{g_{n-1}}^{\min}))} \tag{24}$$

where t_{wave} (see Eq. (20)) is the duration of the injected transient wave at the source, which is about 0.005 s when measured from Fig. 16. Equation (24) provides the minimum distance from the source at which the energy packet of mode n and mode $n-1$ become separated. Applying Eq. (24) to M2 gives $x_2^s = 0.005/(1/670 - 1/865) \approx 15$ m. In fact, Fig. 17a shows that M2 gets separated from M0 and M1 at about 15 m away from the source. For M1, Eq. (24) gives $x_1^s = 0.005/(1/910 - 1/1000) \approx 50$ m, which agrees with Fig. 17c in which M1 is separated from M0 about 50 m from the source.

Figure 18 gives the total area-averaged energy distribution along the pipe at the time $t = 0.7L/a$ (Fig. 18a) and the energy flux variation with time for the case of $f_c = 6800$ Hz measured at 50 m away from the source (Fig. 18b). Figure 18a shows the three energy packets after they are separated from one another. The leading edge of the energy packet of the nth excited mode travels at $V_{gn}^{\max}$ while the trailing edge travels at $V_{gn}^{\min}$. The width of the base of each packet in Fig. 18b provides the time it takes for that packet to pass through the measurement station. Mathematically, this time is given by $x^{mes}/V_{gn_h}^{\min}$ where x^{mes} is the measurement location away from the source and n_h is the highest excited mode number. Consider $f_c = 6800$ Hz and the wave is sampled at 50 m from the source; thus mode M2 takes about $50/410 \approx 1.22\ L/a$ to completely travel through this measurement station. This is in contrast to the case of a resonating probing wave (see Section 5.1) where the tail of the energy extends from the source location to the measurement location (Fig. 14) because the group velocity near cut-off frequency is small and at the cut-off frequency it is zero (Fig. 1). In this case, the required duration to observe the full packet at a certain measurement position tends to infinity.

In Fig. 17c, the M2 waveform is more elongated to the right side (tail of the packet) than to the left side (head of the packet) whereas M0 and M1 waveforms are not. To explain this observation, consider the group velocity plots in Fig. 19. With the FBW of interest, the group velocity for M0 is constant, the group velocity for M1 is close to being linear and changes very little

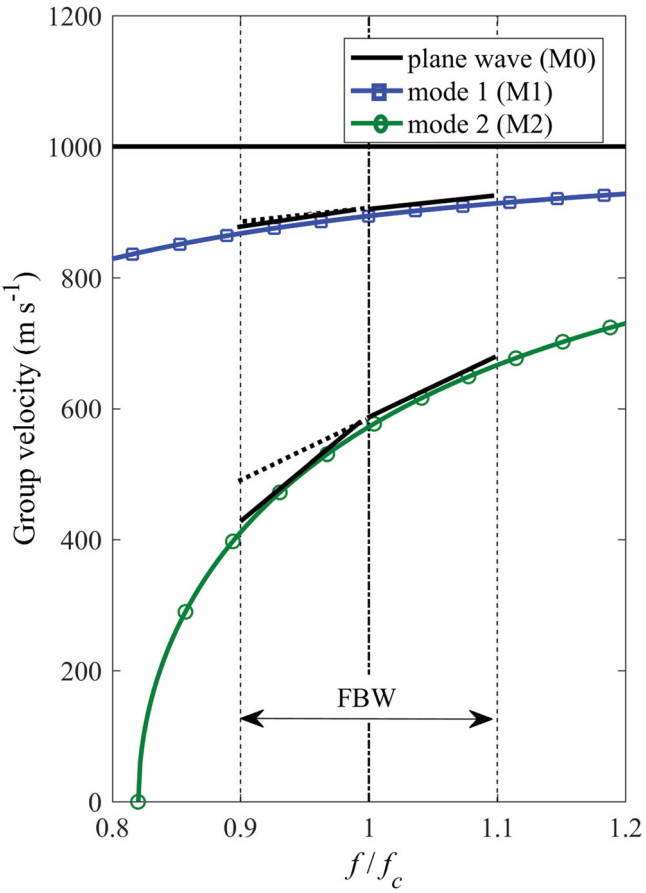

Figure 19 Group velocity variation with the non-dimensional frequency (f/f_c; where $f_c = 6800$ Hz) showing how the M2 group velocity variation is steeper to the left side of the central frequency than to the right side, whereas the variation slope is almost the same for M1

with frequency, but the group velocity of M2 varies strongly with frequency. In addition, the rate of variation with frequency is zero for M0, small but nearly constant for M1 and nonlinear for M2. In fact, the slope of the group velocity for M2 is steep for frequencies below $f_c = 6800$ Hz, but becomes very mild from frequencies larger than this central frequency. The asymmetry of the M2 wave packet seen in Fig. 17 is due to the large variability in group velocity with the FBW being investigated.

To further illustrate the role of group velocity on the shape of a wave packet, another test case with $f_c = 4000$ Hz is shown in Fig. 20. It is clear that M1 is not symmetric with respect to f_c in this case. Again, this is because the M1 group velocity exhibits larger variability within the FBW centred at 4000 Hz. In practice this implies that a mode excited by frequencies that are substantially larger than its cut-off frequency experiences little dispersion but needs to propagate over a large distance before it becomes separated from the other modes. Conversely, a mode that is excited by frequencies larger than but close to its cut-off frequency experiences large dispersion; its packet is not symmetric with respect to the central frequency and propagates only a short distance before becoming separated from the other modes.

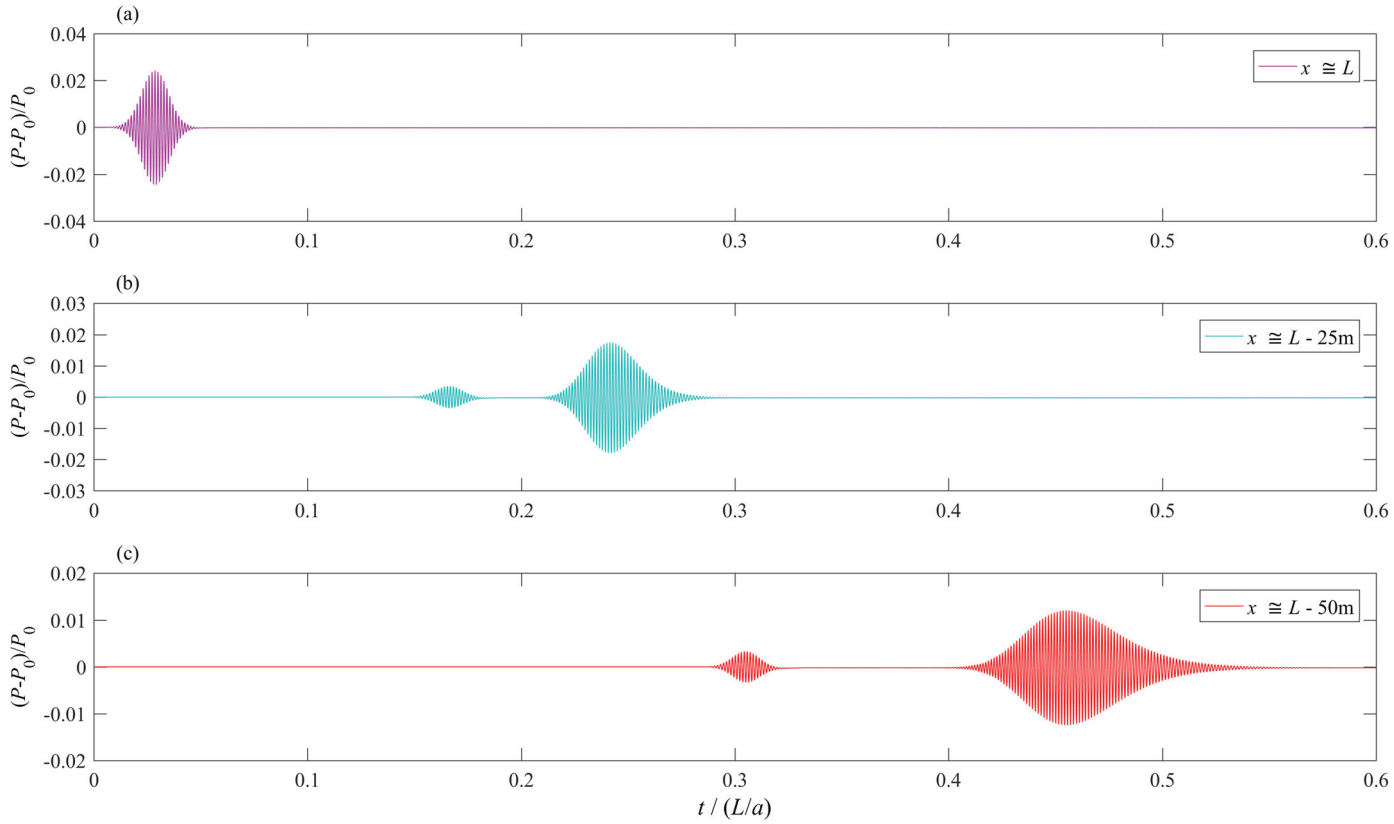

Figure 20 Variation of the pressure signal at the centreline with time for the case $f_c = 4000$ Hz where only M0 and M1 are excited. (a) at $x \approx L$ (near the source); (b) at 25 m away from the source; (c) at 50 m away from the source

6 Conclusions

The physics of acoustic wave behaviour in ducts containing gas/air is well understood, but there is little literature relevant to high-frequency waves in water-filled pipes. The current work studies the propagation of acoustic waves in water pipes to analyse the behaviour of high radial modes when high-frequency waves are injected in a water-filled pipe. When these high-frequency waves are used for multi-scale defect detection in full conduit flow water pipe systems, this study and its insights could help in the effective design of probing signals and the selection or evaluation of signal processing techniques used to analyse the propagating wave signals. Key conclusions of this work are given below:

(1) A Riemann solver scheme provides good accuracy in modelling high-frequency waves. It is able to preserve the physical dispersion of the waves with minimal numerical dissipation.
(2) The resonant response of high-frequency waves is studied and results compare favourably with the properties of 2-D inviscid wave theory where the natural cut-off frequencies are well defined.
(3) At a given location x, the pressure nodes of standing radial waves located at $J_0(k_{rn}r) = 0$ are accurately observed from the numerical results. At these pressure nodes, the pressure is constant, the wave-induced axial velocity is zero and the wave-induced radial velocity is maximal. Knowledge of the locations of these nodes could be useful for locating sensors to maximize information extraction in TBDDM.
(4) The dispersion and multi-path effect of higher modes is analysed. It is shown that the energy contained in higher modes becomes distributed along the pipe in the form of an energy tail that grows longer and more uniform with distance from the source. As a result, when high-frequency waves are injected as probing signals for pipe condition assessment or defect detection, the further the measurement locations are from the source, the longer the measurement time must be to observe the full signal. In addition, it is important to measure close enough to the source to ensure that the wave signal does not become "swamped by noise".
(5) If the injected FBW contains the cut-off frequency for a given mode n, the energy tail of the nth mode is theoretically infinite because the group velocity near the cut-off frequency is very small near, and zero at, the cut-off frequency. However, when the cut-off frequency is not included in the injected FBW, the nth excited mode may be separated from all other excited modes with a finite length of energy tail and the degree of spreading (separation) with distance from the source will depend on its group velocity variation within the injected FBW.
(6) It is found that the size of the radial scale of the wave source (i.e. its diameter relative to the pipe diameter) has a potentially significant influence on the distribution of

input energy across the various excited modes, and, therefore, affects how much energy is carried by the plane (M0) waves. Indeed, it is shown that a small-sized source could reduce the amplitude of the M0 waves, resulting in a reduction in its range of propagation before the signal is no longer discernible. When high-frequency waves are used for TBDDM, and if these methods rely on measuring the plane (M0) waves, then the source size could play a significant role in establishing the distance over which the probing signals might provide useful information about defects. Results of further study into the influence of source size on propagation distance will be provided in a future work.

Acknowledgements

The authors thank Dr D.A. McInnis for the technical and editorial suggestions.

Funding

This study is supported by the Hong Kong Research Grant Council [projects 612712, 612713, T21-602/15R] and by the Postgraduate Studentship.

Notation

A = area integration constant (m^2)
a = acoustic wave speed in water ($m\ s^{-1}$)
B = integration constant (Pa)
D = pipe diameter (m)
D_s = source diameter (m)
E_{Fn} = energy flux of the nth mode ($J\ s^{-1}$)
E_n = total energy per unit wavelength of the nth mode ($J\ m^{-1}$)
f = frequency (Hz)
f_1 = cut-off frequency of the first mode (Hz)
f_2 = cut-off frequency of the second mode (Hz)
f_c = central frequency (Hz)
$\overrightarrow{i}$ = unit vector along the radial direction
$\overrightarrow{j}$ = unit vector along the axial direction
J_0 = Bessel function of order 0 (–)
k = wave number ($rad\ m^{-1}$)
k_{rn} = radial wave number of the nth mode ($rad\ m^{-1}$)
k_{xn} = axial wave number of the nth mode ($rad\ m^{-1}$)
L = length of the pipe (m)
n = radial mode number (–)
N_R = number of discrete finite volumes along the radial direction (–)
N_X = number of discrete finite volumes along the axial direction (–)
P = pressure (Pa)
P_n = pressure of the nth radial mode (Pa)
P_F = transient pressure at the source (Pa)
P_s = pressure amplitude of the generated source (Pa)
r = radial coordinate (m)
R = radius of the pipe (m)
$\boldsymbol{S}$ = vector of terms due to cylindrical coordinate system (–)
t = time (s)
t^{mes} = measurement time (s)
t_p = time period (s)
t_{wave} = duration of the generated transient wave (s)
V_{g_n} = group velocity of the nth mode ($m\ s^{-1}$)
$V_{g_n}^{\max}$ = maximum group velocity of the nth mode ($m\ s^{-1}$)
$V_{g_n}^{\min}$ = minimum group velocity of the nth mode ($m\ s^{-1}$)
V_r = radial velocity ($m\ s^{-1}$)
V_{rn} = radial velocity of the nth mode ($m\ s^{-1}$)
V_x = axial velocity ($m\ s^{-1}$)
V_{xn} = axial velocity of the nth mode ($m\ s^{-1}$)
w = angular frequency ($rad\ s^{-1}$)
w_c = central angular frequency ($rad\ s^{-1}$)
x = axial coordinate (m)
x_n^s = position at which the nth mode is separated from all other excited modes.
α_{rn} = nth zero of Bessel function of order 1 (–)
β = constant defining the FBW (rad)
γ_n = nth pressure amplitude of the left going wave (Pa)
Δr = radial length of the discrete finite volume (m)
Δx = axial length of the discrete finite volume (m)
θ = azimuthal coordinate (rad)
θ_{kn} = propagation angle of the nth mode
λ_n = wavelength of the nth mode (m)
ρ = density ($kg\ m^{-3}$)
υ_n = phase velocity of the nth mode ($m\ s^{-1}$)
φ_n = nth pressure amplitude of the left going wave (Pa)
χ = norm function used to obtain the numerical scheme accuracy (–)

References

Allen, M., Preis, A., Iqbal, M., Srirangarajan, S., Lim, H. B., Girod, L., & Whittle, A. J. (2011). Real-time in-network distribution system monitoring to improve operational efficiency. *Journal American Water Works Association (AWWA)*, *103*(7), 63–75.

Anderson, D., & Barnes, C. (1953). The dispersion of a pulse propagated through a cylindrical tube. *The Journal of the Acoustical Society of America*, *25*(3), 525–528.

Brunone, B., & Ferrante, M. (2001). Detecting leaks in pressurised pipes by means of transients. *Journal of Hydraulic Research*, *39*(5), 539–547.

Chaudhry, M. H. (2014). *Applied hydraulic transients* (3rd ed.). New York, NY: Springer.

Covas, D., Ramos, H., Brunone, B., & Young, A. (2004, March 24–26). *Leak detection in water trunk mains using transient pressure signals: Field tests in scottish water*. International Conference on Pressure Surges, Chester.

Duan, H., Lee, P. J., Kashima, A., Lu, J., Ghidaoui, M., & Tung, Y. (2013). Extended blockage detection in pipes using the system frequency response: Analytical analysis and experimental verification. *Journal of Hydraulic Engineering*, *139*(7), 763–771.

Eichinger, P., & Lein, G. (1992, September 29–October 1). *The influence of friction on unsteady pipe flow*. Proceedings of the International conference on unsteady flow and fluid transients, Durham, pp. 41–50.

Ghidaoui, M. S. (2004). On the fundamental equations of water hammer. *Urban Water Journal*, *1*(2), 71–83.

Hartig, H. E., & Swanson, C. E. (1938). "Transverse" acoustic waves in rigid tubes. *Physical Review*, *54*(8), 618–626.

Hirsch, C. S. (Ed.). (2007). *Numerical computation of internal and external flows: Fundamentals of computational fluid dynamics* (2nd ed.). Amsterdam: Elsevier, Butterworth-Heinemann.

Hong Kong Water Supplies Department (WSD). (2015). *Private communication*.

Jiang, G., & Shu, C. W. (1996). Efficient implementation of weighted ENO schemes. *Journal of Computational Physics*, *126*, 202–228.

Kokossalakis, G. (2006). *Acoustic data communication system for in-pipe wireless sensor networks* (Doctoral dissertation). Massachusetts Institute of Technology.

Lee, P. J., Duan, H., Ghidaoui, M., & Karney, B. (2013). Frequency domain analysis of pipe fluid transient behaviour. *Journal of Hydraulic Research*, *51*(6), 609–622.

Lee, P. J., Duan, H., Tuck, J., & Ghidaoui, M. (2015). Numerical and experimental study on the effect of signal bandwidth on pipe assessment using fluid transients. *Journal of Hydraulic Engineering*, *141*(2), 04014074.

Lee, P. J., Vítkovský, J. P., Lambert, M. F., Simpson, A. R., & Liggett, J. A. (2008). Discrete blockage detection in pipelines using the frequency response diagram: Numerical study. *Journal of Hydraulic Engineering*, *134*(5), 658–663.

Liggett, J. A., & Chen, L. (1994). Inverse transient analysis in pipe networks. *Journal of Hydraulic Engineering*, *120*(8), 934–955.

Louati, M. (2016). *In-depth study of plane wave-blockage interaction and analysis of high frequency waves behaviour in water-filled pipe systems* (Doctoral dissertation). HKUST. Retrieved from http://lbezone.ust.hk/bib/b1618552

Louati, M., & Ghidaoui, M. S. (2015, June 28–July 3). *Wave blockage interaction in pipes*. E-proceedings of the 36th IAHR World Congress, The Hague.

Meniconi, S., Brunone, B., Ferrante, M., Capponi, C., Carrettini, C., Chiesa, C., & Lanfranchi, E. (2015). Anomaly pre-localization in distribution–transmission mains by pump trip: Preliminary field tests in the milan pipe system. *Journal of Hydroinformatics*, *17*(3), 377–389.

Meniconi, S., Duan, H., Lee, P., Brunone, B., Ghidaoui, M., & Ferrante, M. (2013). Experimental investigation of coupled frequency and time-domain transient test–based techniques for partial blockage detection in pipelines. *Journal of Hydraulic Engineering*, *139*(10), 1033–1040.

Miles, J. (1944). The reflection of sound due to a change in cross section of a circular tube. *The Journal of the Acoustical Society of America*, *16*(1), 14–19.

Mitra, A., & Rouleau, W. (1985). Radial and axial variations in transient pressure waves transmitted through liquid transmission lines. *Journal of Fluids Engineering*, *107*(1), 105–111.

Ohwada, T., Adachi, R., Xu, K., & Luo, J. (2013). On the remedy against shock anomalies in kinetic schemes. *Journal of Computational Physics*, *255*, 106–129.

Pezzinga, G. (1999). Quasi-2-D model for unsteady flow in pipe networks. *Journal of Hydraulic Engineering*, *125*(7), 676–685.

Pezzinga, G. (2000). Evaluation of unsteady flow resistances by quasi-2-D or 1-D models. *Journal of Hydraulic Engineering*, *126*(10), 778–785.

Richards, S. K., Zhang, X., Chen, X., & Nelson, P. A. (2004). The evaluation of non-reflecting boundary conditions for duct acoustic computation. *Journal of Sound and Vibration*, *270*(3), 539–557.

Rienstra, S. W., & Hirschberg, A. (2004). *An introduction to acoustics*. Eindhoven: Eindhoven University of Technology.

Rochester, N. (1941). The propagation of sound in cylindrical tubes. *The Journal of the Acoustical Society of America*, *12*(4), 511–513.

Sattar, A. M., Chaudhry, M. H., & Kassem, A. A. (2008). Partial blockage detection in pipelines by frequency response method. *Journal of Hydraulic Engineering*, *134*(1), 76–89.

Silva-Araya, W. F., & Chaudhry, M. H. (1997). Computation of energy dissipation in transient flow. *Journal of Hydraulic Engineering*, *123*(2), 108–115.

Thompson, K. W. (1987). Time dependent boundary conditions for hyperbolic systems. *Journal of Computational Physics*, *68*(1), 1–24.

Thompson, K. W. (1990). Time-dependent boundary conditions for hyperbolic systems, II. *Journal of Computational Physics*, *89*(2), 439–461.

Tijdeman, H. (1975). On the propagation of sound waves in cylindrical tubes. *Journal of Sound and Vibration*, *39*(1), 1–33.

Toro, E. F. (2009). *Riemann solvers and numerical methods for fluid dynamics: A practical introduction* (3rd ed.). New York: Springer Science & Business Media.

Vardy, A. E., & Hwang, K. (1991). A characteristics model of transient friction in pipes. *Journal of Hydraulic Research*, *29*(5), 669–684.

Vítkovský, J. P., Simpson, A. R., & Lambert, M. F. (2000). Leak detection and calibration using transients and genetic algorithms. *Journal of Water Resources Planning and Management*, *126*(4), 262–265.

Wang, X., Lambert, M. F., & Simpson, A. R. (2005). Detection and location of a partial blockage in a pipeline using damping of fluid transients. *Journal of Water Resources Planning and Management*, *131*(3), 244–249.

Xu, K., & Li, Z. W. (2001). Dissipative mechanism in godunov-type schemes. *International Journal for Numerical Methods in Fluids*, *37*, 1–22.

Zhao, M., Duan, H. F., & Ghidaoui, M. S. (2016). Transient wave and extended blockage interaction in pipe flows. *Journal of Hydraulic Research, IAHR*. (conditionally accepted).

Zhao, M., & Ghidaoui, M. S. (2003). Efficient quasi-two-dimensional model for water hammer problems. *Journal of Hydraulic Engineering*, *129*(12), 1007–1013.